

STRAINED GERMANIUM TECHNOLOGY
FOR ON-CHIP OPTICAL INTERCONNECTS

A DISSERTATION
SUBMITTED TO THE DEPARTMENT OF ELECTRICAL ENGINEERING
AND THE COMMITTEE ON GRADUATE STUDIES
OF STANFORD UNIVERSITY
IN PARTIAL FULFILLMENT OF THE REQUIREMENTS
FOR THE DEGREE OF
DOCTOR OF PHILOSOPHY

Donguk Nam

December 2013

Abstract

Since the invention of the first transistor over half a century ago, transistor scaling has led the semiconductor industry to blossom. Despite the improved performance of scaled transistors, however, the computational speed of integrated circuits (IC) has now become limited by their electrical interconnects. To alleviate this performance bottleneck in ICs, optical interconnects, which have already revolutionized long-haul communications, have recently gained much attention for on-chip applications. Over the past decade many of the key constituents of an on-chip optical interconnect system, such as high-performance photodetectors and modulators, have been demonstrated on a silicon-compatible platform. However, an efficient light source remains particularly challenging: silicon and silicon-compatible materials such as germanium (Ge) are not readily suitable for light emission because their band gaps are indirect. It has been proposed to use tensile strain to make Ge's band gap direct and therefore suitable for light emission, however experimental realization has thus far been lacking.

In this dissertation, we focus on developing an efficient silicon-compatible light emitter based on strained Ge technology. Starting from theoretical calculations

showing how tensile strain can improve the light emission efficiency of Ge, we present several approaches for enhancing light emission from highly strained Ge on a CMOS-compatible platform. In the first part, we describe a thin film membrane technique in which a large residual stress in a tungsten layer is used as a stressor to induce a biaxial strain in a Ge membrane, upon which we have fabricated optoelectronic devices. In the second part, we introduce an approach to induce uniaxial strain that can potentially create a direct band gap in Ge wire using geometrical amplification of a small pre-existing strain. Lastly, we present a novel way to mimic double-heterostructure behavior within a single material, further enhancing light emission from Ge by capturing photo-generated carriers within a strain-induced potential well. Throughout this dissertation, we discuss the implications of these experimental achievements towards creating an efficient Ge laser for use in silicon-compatible optical interconnects.

Acknowledgements

Last 4 years at Stanford working towards a PhD degree has truly been the most fruitful time of my life and it would have never been possible without so many people around me who fully supported me. Firstly, I would like to express my deepest gratitude to my advisor, Prof. Krishna Saraswat, for having been always encouraging me even when I did not believe in myself. I feel truly blessed to have worked with such a sincere mentor who tremendously influenced not only my academic life, but also how I view everything.

I am also thankful to my co-advisor, Prof. Jelena Vuckovic. Taking her classes and talking to her personally has indeed opened my eyes to the area of optical devices and her passion for research has always motivated me. I would also like to thank Prof. Mark Brongersma for all the great advice that helped me improve this dissertation. I am also grateful to Prof. James Harris for graciously sharing with me all his knowledge on germanium-based optoelectronics. I would also like to thank Prof. Ted Kamins for his selfless instructions and his enthusiasm towards research that has

always inspired me. I am also thankful to Dr. Raj Dutt, CEO of APIC and PhotonIC, for supporting my PhD financially and intellectually.

I am also greatly indebted to all my collaborators and the Saraswat group members who always shared their expertise very generously. Interacting with and learning from experts in their field indeed kept this research project moving forward. I would especially like to thank Dave Sukhdeo for being the greatest collaborator. Discussing ideas and results with him has immensely helped me become a better researcher. I am also very thankful to all the SNF staff members for sharing all their knowledge on device fabrication. I would also like to express my gratitude to my dear friends and the members of SGBT (Stanford Friday Night Tennis Club) for being the best buddies both on and off court.

Also, I am sincerely thankful to my parents and my older sister for their unconditional love over the past 30 years. Without their support and encouragements, I would not have been able to make it this far.

Finally, I would like to thank my beloved family, Tyler Wonwoo Nam and Nuri Kim. Because of the lovely smiles my family has given me everyday, I truly enjoyed this journey which otherwise might have been sometimes tiring. I wholeheartedly dedicate this dissertation to my family.

Table of Contents

Abstract.....	iv
Acknowledgements	vi
Table of Contents	viii
List of Figures.....	xii
Chapter 1: Introduction.....	1
1.1 Motivation	1
1.2 Organization of the Dissertation.....	6
Chapter 2: Background on Strained Ge Technology.....	8
2.1 Introduction	8
2.2 Strained Ge for an Efficient Light Source.....	9
2.2.1 The Need of Strain to Improve Optical Properties of Ge.....	9
2.2.2 Theoretical Calculation of Band Gap Energy versus Strain.....	12
2.2.3 Theoretical Calculation of Improved Light Emission from Ge.....	13

2.3 Literature Review and Direction of Our Work.....	15
Chapter 3: Biaxially Strained Ge Membrane Integrated on a Si Substrate	20
3.1 Introduction	20
3.2 Fabrication of Strained Ge Membrane	21
3.3 Characterization of Strained Ge Membrane.....	24
3.3.1 Mechanical Property Characterization	25
3.3.2 Optical Property Characterization	26
3.4 Theoretical Modeling for Population Inversion	27
3.5 Realization of Optoelectronic Devices.....	29
3.5.1 Integration of PN Diodes on Strained Membranes.....	29
3.5.2 Current-Voltage Characteristics	31
3.5.3 Photocurrent Measurement.....	32
3.5.4 Electroluminescence Measurement.....	34
3.6 Proposal for a Laser Structure	36
3.6.1 Optical Cavity Simulation	36
3.6.2 Lasing Threshold Calculation.....	37
3.7 Conclusion	40
Chapter 4: Uniaxially Strained Ge Wires via CMOS-Compatible Approach.....	42
4.1 Introduction	42

4.2 Ge-on-Insulator Wafer Fabrication	43
4.3 Creation of Uniaxially Strained Ge Wires.....	48
4.3.1 Working Principle of Geometrical Amplification of Strain	48
4.3.2 Strain and Band Structures	51
4.4 Carrier Dynamics Study	53
4.4.1 Strain-Dependent PL Measurement	53
4.4.2 Polarization-Dependent PL Measurement.....	55
4.4.3 Temperature-Dependent PL Measurement.....	57
4.4.4 Excitation-Dependent PL Measurement.....	58
4.5 Theoretical Modeling for a Low-Threshold Ge Laser	61
4.6 Conclusion	63
Chapter 5: Strain-Induced Pseudo-Heterostructure with Tunable Band Profiles.....	65
5.1 Introduction	65
5.2 Creation of Strain-Induced Potential Wells.....	67
5.3 Light Emission from Strain-Induced Potential Wells	75
5.3.1 Spatially Confined Light Emission	75
5.3.2 Wavelength-Shifted, Enhanced Light Emission.....	78
5.3.3 PL Emission Dependence on Excitation Locations.....	83
5.4 Conclusion	85

Chapter 6: Conclusions & Future Works	87
Bibliography	90

List of Figures

Figure 1.1 Prediction in 1982 of time delay of interconnections in different materials and average gate delay versus year	2
Figure 1.2 Optical communication systems at different length scales	3
Figure 1.3 Use of optics for communications of various length scales.....	4
Figure 1.4 Time delay and energy consumption of various interconnection schemes..	4
Figure 1.5 Schematic diagram of an optical interconnects system	5
Figure 2.1 Monolithic Ge-on-Si Avalanche photodetector	9
Figure 2.2 Absorption coefficients for various materials.....	10
Figure 2.3 Schematic diagrams of band structures of unstrained Ge and tensile strained Ge	11
Figure 2.4 Band gap energies for various band-to-band transitions versus biaxial tensile strain.....	13
Figure 2.5 Percentage of electrons in the Γ valley versus strain for Ge with $1 \times 10^{18} \text{ cm}^{-3}$ n-type doping.....	14

Figure 2.6 Internal quantum efficiency of Ge with $1 \times 10^{18} \text{ cm}^{-3}$ n-type doping versus strain for various SRH lifetimes	15
Figure 2.7 Schematic diagrams of strain development due to thermal expansion mismatch.....	16
Figure 2.8 Schematic of mechanical bending setup	17
Figure 2.9 Strained Ge nanomembrane on a polyimide film	18
Figure 3.1 Fabrication process flow for highly strained Ge membranes	23
Figure 3.2 SEM and 3D profile of a strained Ge membrane.....	23
Figure 3.3 Normalized Raman spectra for membranes under various amounts of strain	25
Figure 3.4 Room temperature PL spectra for membranes under various amounts of strain	26
Figure 3.5 Required injection carrier density for population inversion versus strain for different n-type doping concentration	27
Figure 3.6 Schematic diagram of a strained Ge PN diode	30
Figure 3.7 Optical image of a strained PN diode showing a deflected active region..	30
Figure 3.8 Current-voltage characteristics of PN diodes on several highly strained membranes.....	31
Figure 3.9 Normalized photocurrents from strained PN diodes.....	33
Figure 3.10 Normalized electroluminescence spectra.....	34

Figure 3.11 Proposal of a laser structure	37
Figure 3.12 Theoretical modeling for a low-threshold Ge VCSEL	39
Figure 4.1 Cross-sectional TEM image of epitaxially grown Ge film on Si.....	44
Figure 4.2 Cross-sectional TEM images of GOI.....	45
Figure 4.3 Plan-view TEM images of Ge film before and after CMP processing	45
Figure 4.4 Process flow for GOI wafer fabrication	47
Figure 4.5 Fabrication process flow for uniaxially strained Ge wires	48
Figure 4.6 SEM images and simulation results of uniaxially strained Ge wires.....	50
Figure 4.7 Raman measurements and schematic of band structures.....	52
Figure 4.8 Strain-dependent PL measurement	53
Figure 4.9 Polarization-dependent PL measurement.....	56
Figure 4.10 Temperature-dependent PL measurement	58
Figure 4.11 Excitation-dependent PL measurement	60
Figure 4.12 Quantitative study of carrier dynamics	61
Figure 4.13 Theoretical modeling for a laser with uniaxially strained Ge as a gain medium	62
Figure 5.1 Strain-induced pseudo-heterostructure nanowires	69
Figure 5.2 Finite-element COMSOL simulations of various pseudo-heterostructure designs	70

Figure 5.3 Pseudo-heterostructure nanowires with custom-designed band profiles at the nanoscale	73
Figure 5.4 Raman spectra for active regions under various amounts of strain	74
Figure 5.5 Spatially confined light emission from strain-induced potential wells.....	76
Figure 5.6 2D PL map comparison between shallow and deep potential wells.....	76
Figure 5.7 Enhanced and wavelength-shifted light emission from the strain-induced potential wells.....	78
Figure 5.8 PL emission dependence on excitation locations.....	84

Chapter 1

Introduction

1.1 Motivation

Since the introduction of the first transistor over half a century ago, the advances in device physics and fabrication technology have been enabling transistor scaling in order to enhance its speed and to increase device packing density in integrated circuits (IC) [1]. While this scaling of individual logic elements has made tremendous progress, electrical interconnects for communications between devices started causing the performance degradation of IC [2]. For example, as the scaling of electrical wires as well as increasing complexity of wiring increases the RC time delay, computational speed of IC became limited by interconnects, not by individual devices as predicted 3 decades ago in Figure 1.1 [2]. In addition, energy consumption by electrical

interconnects has been constantly increasing with device scaling and is thereby contributing more than 50% of the total dynamic power consumption of microprocessors [3].

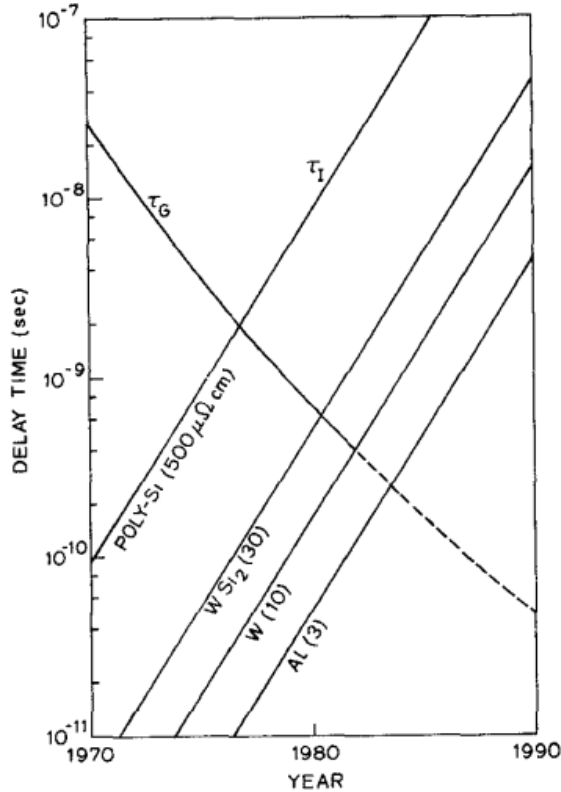


Figure 1.1 Prediction in 1982 of time delay of interconnections in different materials and average gate delay versus year. [2]

While communications within IC became more problematic as technology advances, long-haul communications have been revolutionized by fiber-optic communication systems which transmit information by sending modulated light

through an optical fiber. Because optical communications have several advantages over the conventional electrical communications such as low signal attenuation, ability to transmit several channels on a single link, etc., they have been successfully adapted into systems of smaller scales as shown in Figure 1.2 and 1.3 [4], [5]. As this trend continued, researchers started searching for hope of alleviating the performance bottleneck of IC due to electrical interconnects by employing on-chip optical interconnects [6]. Indeed, as shown in Figure 1.4 [7], system-level simulations have predicted that optical interconnects might outperform electrical counterparts in terms of computational speed and energy consumption when on-chip optical devices meet certain requirements which have been laid out in detail in Ref. [8].

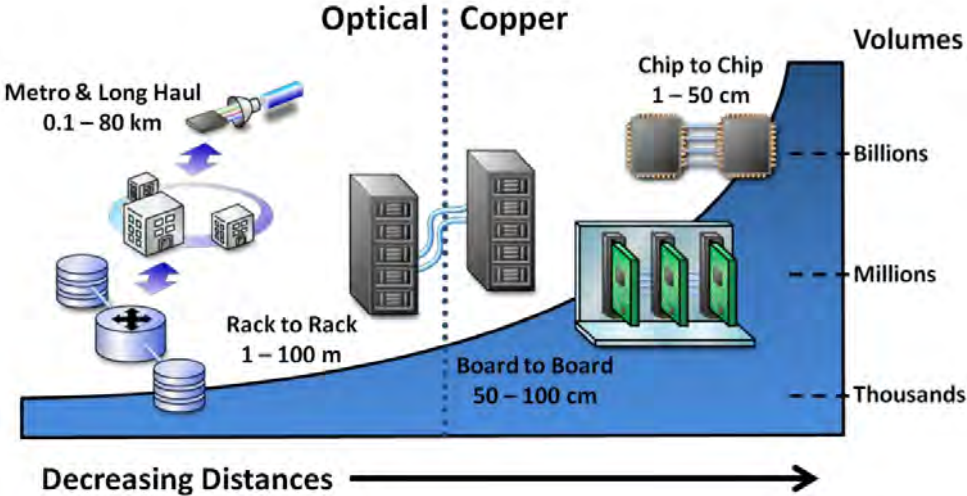


Figure 1.2 Optical communication systems at different length scales. [4]

	Internet, Wide Area Network	Local Area Network	Rack-to-Rack	Card-to-Card	On-Card	On- MCM	On-Chip
							
Distance	multi-km	10 - 2000 m	30+ m	1 m	0.1 - 0.3 m	5 - 100 mm	0.1 - 10 mm
Number of lines	1	1 - 10	~100	~100-1000	~1000	~10'000	~100'000
Use of optics	Since the 80s and the early 90s	Since the late 90s	Now	2010+	2010-2015	Probably after 2015	Later, if ever

Figure 1.3 Use of optics for communications of various length scales. [5]

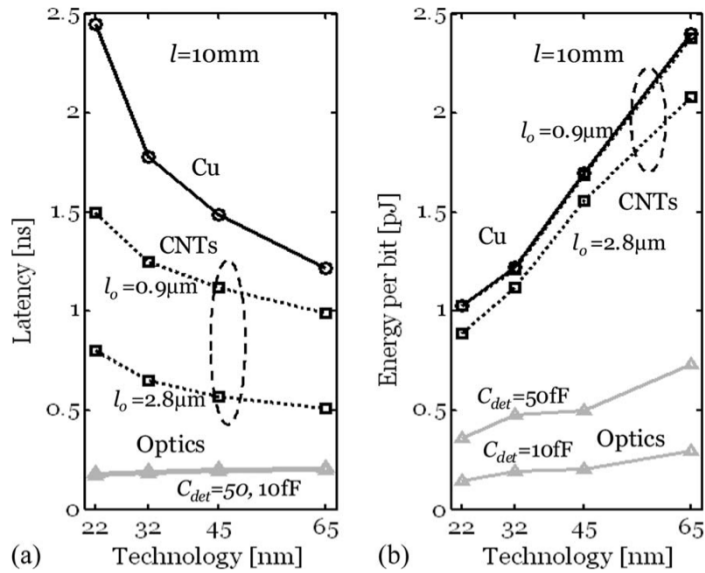


Figure 1.4 Time delay and energy consumption of various interconnection schemes. [7]

Figure 1.5 presents a schematic diagram of an optical interconnects system and shows four main optical devices in white boxes: laser, modulator, waveguide and

photodetector [9]. While conventional interconnects transmit signals directly from one logic device to another via electrical wires, in an optical interconnects system, electrical signals from the logic device are sent to the modulator in order to modulate a continuous-wave (CW) light from the laser into optical signals. The transmitted light via the waveguide can then be detected by the photodetector and converted back to electrical signals [9].

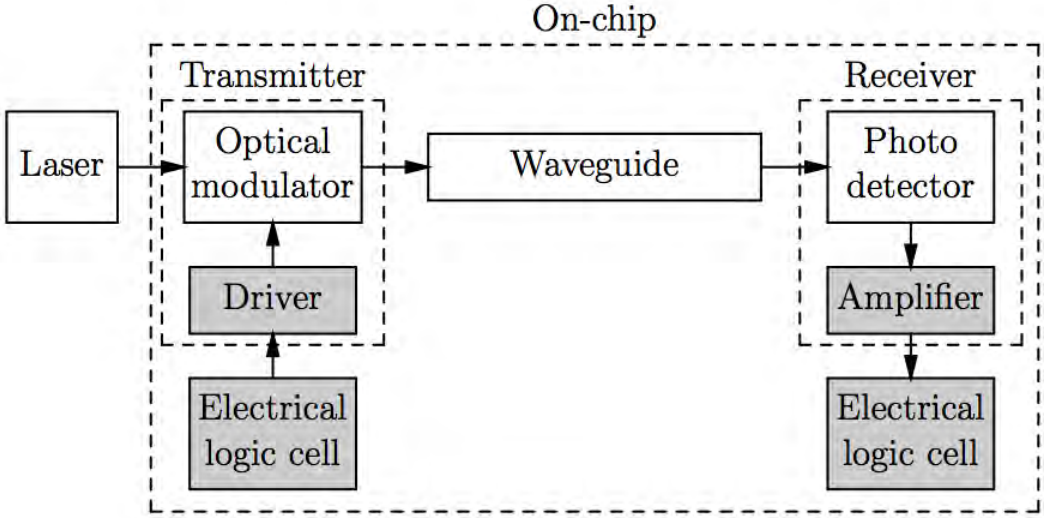


Figure 1.5 Schematic diagram of an optical interconnects system. [9]

Such a system that needs both electronic and optical components on a chip requires monolithic integration of each component for cost-effective application. In this regard, the use of germanium (Ge) for building optical components has recently attracted much attention because Ge can be monolithically integrated on silicon (Si). Therefore, researchers have been extensively working on Ge-based optical devices in

order to realize monolithically integrated optical interconnects system. While research on other essential optical components such as modulators, waveguides and detectors has shown tremendous progress [10]–[14], an efficient Ge light source remains particularly challenging due to its indirect band gap. Because the global minimum of the conduction band does not lie at the Brillouin zone center, the probability of radiative recombination of the electron-hole pairs is quite low. Fortunately, however, theoretical calculations have recently predicted that the optical properties of Ge can be drastically improved by applying strain [15], [16] because the energy difference between the direct Γ valley and the indirect L valley can be reduced by tensile strain due to the different deformation potential parameters in the two valley [17]. Therefore, this dissertation focuses on developing platform technologies for highly strained Ge devices for an efficient light source for on-chip optical interconnects.

1.2 Organization of the Dissertation

Chapter 2 introduces underlying knowledge behind strained Ge technology. We will present theoretical calculations showing how electronic band structure of Ge is modified as strain is applied. Based upon these calculations, we will show how optical properties of Ge can be improved. The chapter will conclude with an overview of previous research effort on straining Ge to improve its optical properties.

Chapter 3 focuses on the fabrication and the optical characterization of Ge membranes under a large biaxial tensile strain. A simulation result showing the

reduction of the required injection carrier density for population inversion is presented. The chapter will conclude with a demonstration of device integration on highly strained Ge membranes.

Chapter 4 discusses a fully CMOS-compatible method to achieve a large uniaxial tensile strain in Ge wires. We present a comprehensive study of carrier dynamics in strained Ge wires via polarization-, temperature- and excitation-dependent photoluminescence (PL) measurements. An implication of a large uniaxial strain in Ge towards creating an efficient Ge light source is presented via theoretical modeling.

Chapter 5 presents a novel concept of strain-induced pseudo-heterostructures which may be critical for achieving an efficient Ge laser. The mechanism responsible for the enhanced PL from the strain-induced potential wells is discussed in detail.

Chapter 6 concludes this dissertation with a brief summary of the key achievements and offers directions for future works.

Chapter 2

Background on Strained Ge Technology

2.1 Introduction

In this chapter, we will discuss strained Ge technology for on-chip optical interconnects, especially focusing on the light source. As strain is a particularly promising method to improve the optical properties of Ge, the effect of strain on the Ge band structures as well as the carrier dynamics in Ge is discussed using theoretical calculations. We will briefly give an overview of previous works on strained Ge by other researchers and, finally, we will conclude this chapter by presenting the directions of our work on strained Ge.

2.2 Strained Ge for an Efficient Light Source

2.2.1 The Need of Strain to Improve Optical Properties of Ge

In order to realize the integration of optical interconnects with silicon circuits, Ge has recently gained an increasing amount of interest because of its complete compatibility with conventional CMOS processes and because of its superior optical properties compared to Si. As shown in Figure 2.1, for example, high-performance Ge-on-Si photodetectors have been successfully demonstrated [18]–[22] because Ge has a much higher optical responsivity than Si over a wide wavelength range as shown in Figure 2.2 [23].

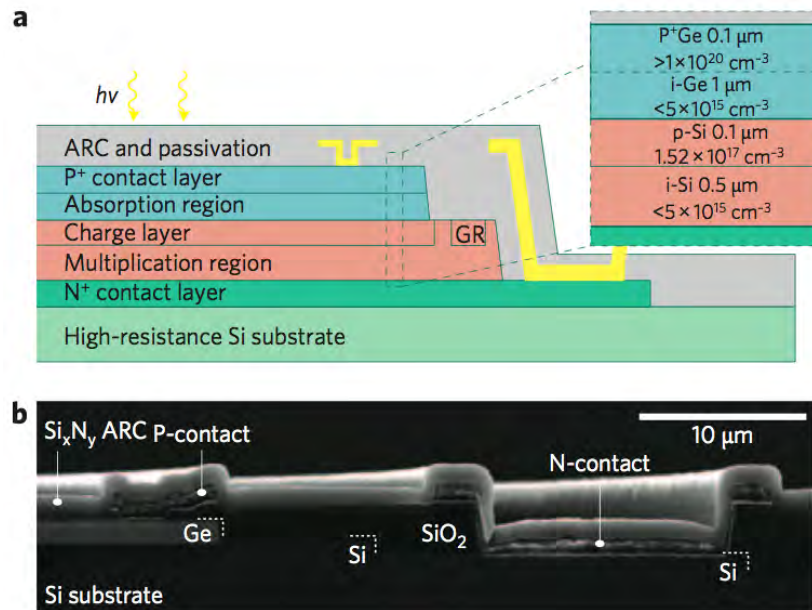


Figure 2.1 Monolithic Ge-on-Si Avalanche photodetector. (a) Schematic diagram. (b) Scanning electron micrograph (SEM).

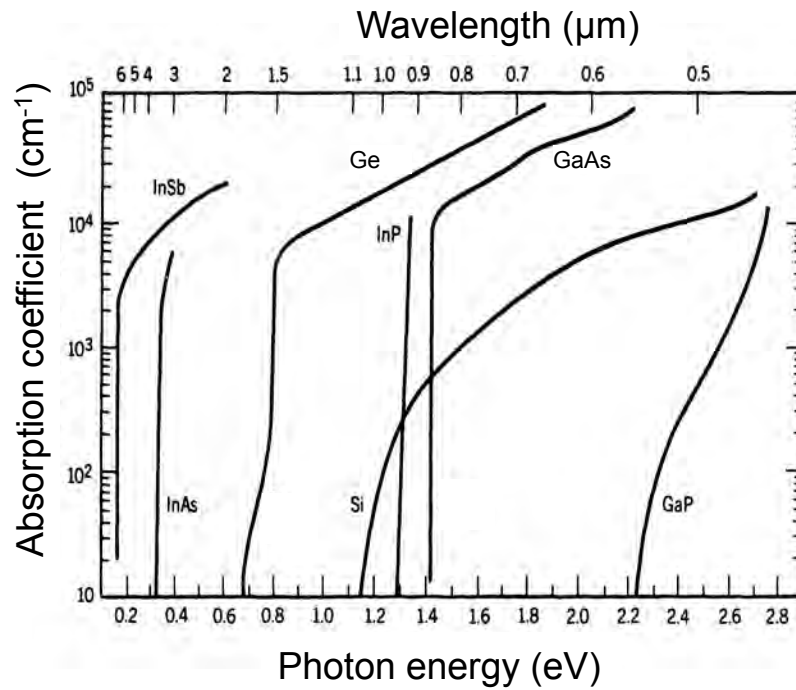


Figure 2.2 Absorption coefficients for various materials. [23]

Unlike a hopeful situation for light detection in Ge, however, light emission in Ge has been considered a formidable task owing to its indirect band gap nature. As shown in Figure 2.3, the band structure of unstrained Ge has a global minimum of the conduction band at the L-point edge of the Brillouin zone. Therefore, most of the injected electrons are pumped into the lower indirect L valley due to the Fermi-Dirac distribution, and these electrons recombine with holes via non-radiative recombination [24].

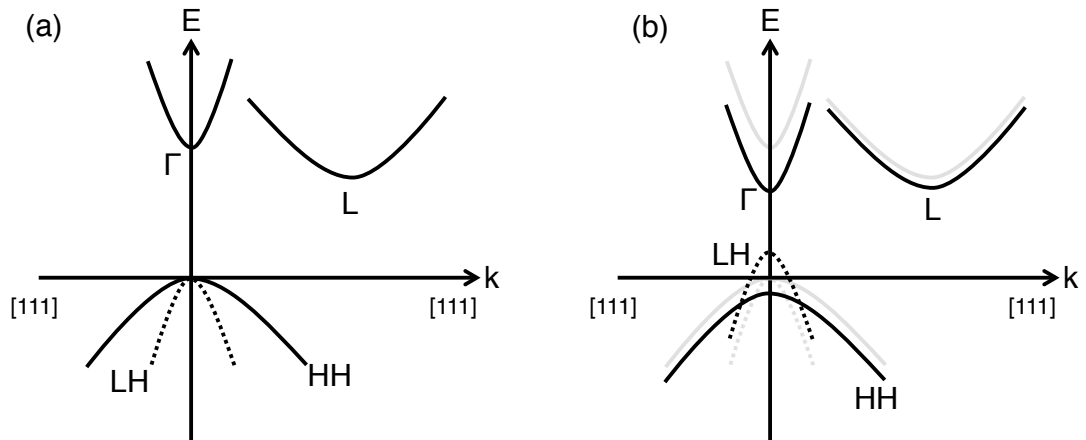


Figure 2.3 Schematic diagrams of band structures of (a) unstrained Ge and (b) tensile strained Ge.

Fortunately, however, the energy difference between the direct Γ valley and the indirect L valley is only 140 meV [17]. Recently, researchers have proposed several methods to overcome this energy difference, such as employing heavy n-type doping, alloying with tin (Sn) and applying tensile strain [25]–[39]. Of these strategies employed to improve the optical properties of Ge, applying a large tensile strain to Ge is particularly promising. As shown in Figure 2.3, biaxial tensile strain reduces the energy difference between the direct Γ valley and the indirect L valley [40]–[49]. As a result, the fraction of the injected electrons into the direct Γ valley can be significantly increased, thereby improving the light emission efficiency in Ge. In addition, strain causes the splitting of the two degenerate bands at the maximum of the valence band, the heavy- and the light-hole bands. This strain-induced valence band splitting is particularly helpful in lowering the lasing threshold because the density-of-states

(DOS) near the top of the valence band can be reduced which leads to the reduction of the amount of hole injection required for population inversion [25].

2.2.2 Theoretical Calculation of Band Gap Energy Versus Strain

Using deformation potential theory [17], we calculated how band gap energies are changed as biaxial tensile strain is applied. As shown in Figure 2.4, unstrained Ge shows band gap energies of 0.8 eV and 0.66 eV for the direct band gap and the indirect band gap, respectively. As the two valence bands, the heavy- and the light-hole bands, are degenerate without strain, there are only two band gap energies for unstrained Ge. As biaxial strain is applied to Ge, however, there exist four distinct band gap energies: the direct Γ valley to the heavy-hole band (c Γ -HH), the indirect L valley to the heavy-hole band (cL-HH), the direct Γ valley to the light-hole band (c Γ -LH) and the indirect L valley to the light-hole band (cL-LH). As mentioned previously, the energy difference between the direct Γ valley and the indirect L valley becomes smaller with higher strain. Interestingly, beyond $\sim 1.7\%$ strain, the direct Γ valley becomes lower than the indirect L valley, which means Ge can be essentially transformed into the direct band gap material [16], [32].

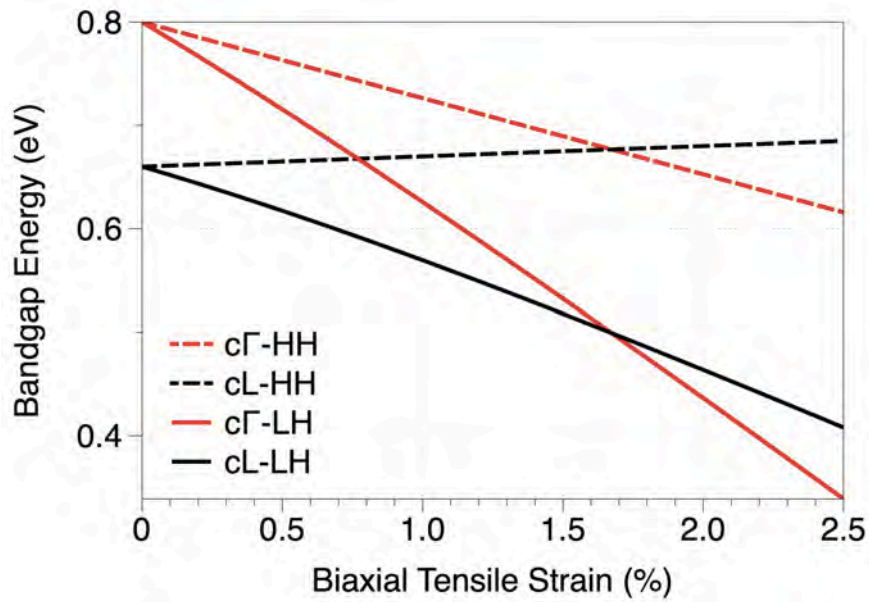


Figure 2.4 Band gap energies for various band-to-band transitions versus biaxial tensile strain.

2.2.3 Theoretical Calculation of Improved Light Emission from Ge

Based upon the band gap energy calculation, we studied the carrier dynamics in strained Ge. Considering the Fermi-Dirac distribution, the different DOS and energy levels of two conduction valleys, we calculated how the percentage of the electron population in the direct Γ valley changes as a function of strain as shown in Figure 2.5. For Ge with $1 \times 10^{18} \text{ cm}^{-3}$ n-type doping, only $<0.01\%$ of total electrons in the conduction band populate the direct Γ valley. However, as the energy difference between two conduction valleys becomes smaller with biaxial strain, the electron population in the direct Γ valley can be significantly increased. It is interesting to note that even at $\sim 2\%$ strain where the direct Γ valley is lower than the indirect L valley,

the electron population in the direct Γ valley for intrinsic Ge is still $\sim 5\%$ because of the much greater DOS in the indirect L valley.

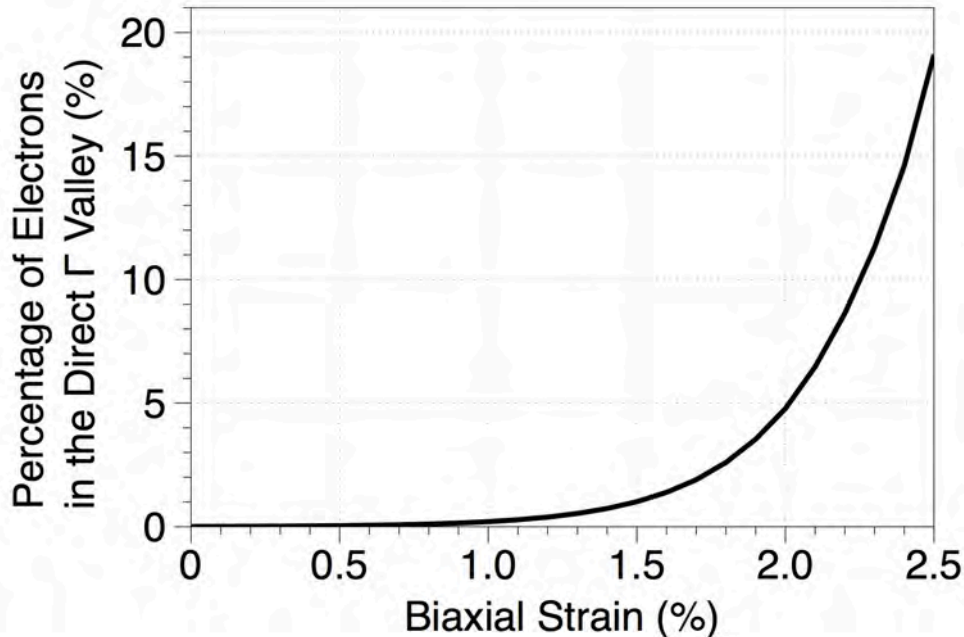


Figure 2.5 Percentage of electrons in the Γ valley versus strain for Ge with $1 \times 10^{18} \text{ cm}^{-3}$ n-type doping.

Figure 2.6 shows how internal quantum efficiency (IQE) of Ge can be improved as a function of biaxial tensile strain for various Shockley-Read-Hall (SRH) carrier lifetimes. As the strain increases the percentage of electrons in the direct Γ valley that can radiatively recombine, and the IQE, which is the ratio of the radiative recombination rate to the total recombination rate, can be also increased with strain. It is worth noting that the longer SRH lifetime can also significantly improve the IQE by reducing the non-radiative recombination rate.

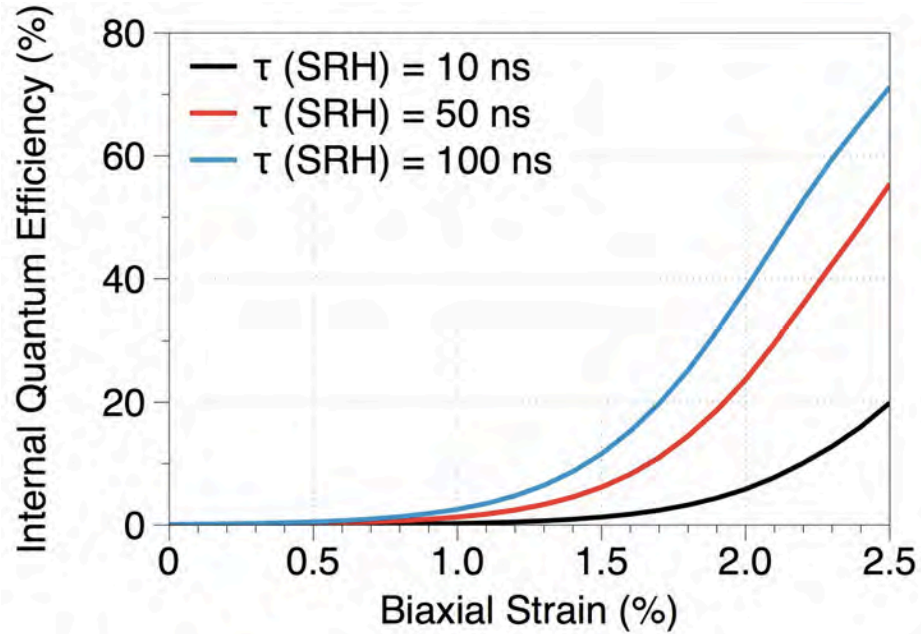


Figure 2.6 Internal quantum efficiency of Ge with $1 \times 10^{18} \text{ cm}^{-3}$ n-type doping versus strain for various SRH lifetimes.

2.3 Literature Review and Direction of Our Work

Since theoretical calculations have revealed the feasibility of strained Ge as an efficient light emitter, a number of research groups have been trying to experimentally demonstrate the improved optical properties of Ge by employing various methods to strain the material.

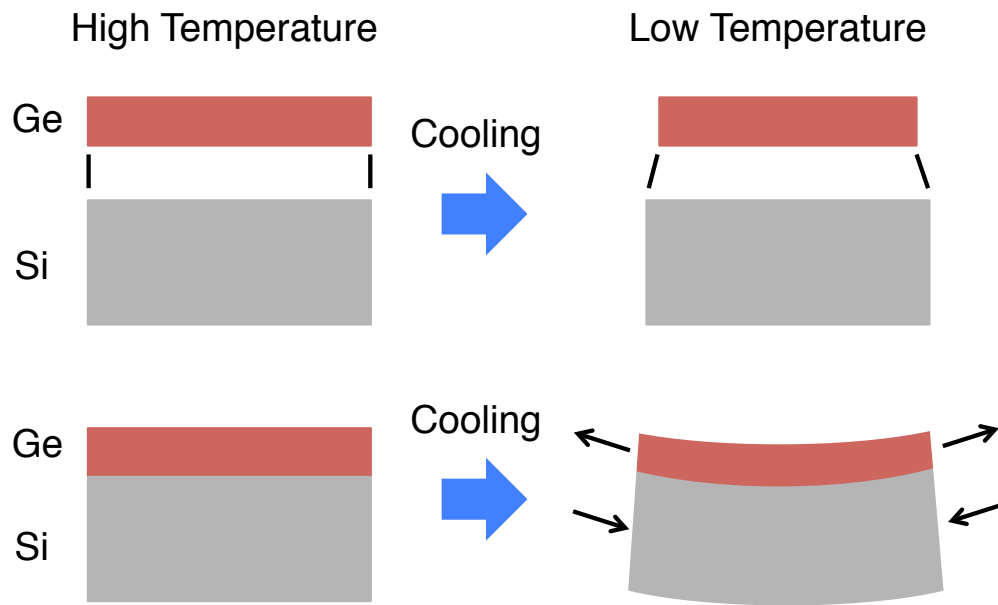


Figure 2.7 Schematic diagrams of strain development due to thermal expansion mismatch.

An initial effort made by many researchers was to take advantage of the thermal expansion mismatch between Si and Ge [50]. When Ge is epitaxially grown on a Si substrate, high temperature annealing is typically required to reduce the density of the threading dislocation in Ge caused by the large lattice mismatch between Si and Ge [51]–[53]. When the wafer cools down from high temperature at ~ 825 °C, a smaller amount of biaxial tensile strain (generally $\sim 0.2\%$) is accumulated due to the large thermal expansion mismatch between Ge and Si as shown in Figure 2.7 [50]. Using a combination of this strain and an indirect valley filling effect from heavy n-type doping, light emission by both optical and electrical pumping has been demonstrated

[54], [55]. However, the maximum strain achievable by this method was unfortunately very low, thereby limiting the improvement of light emission from Ge.

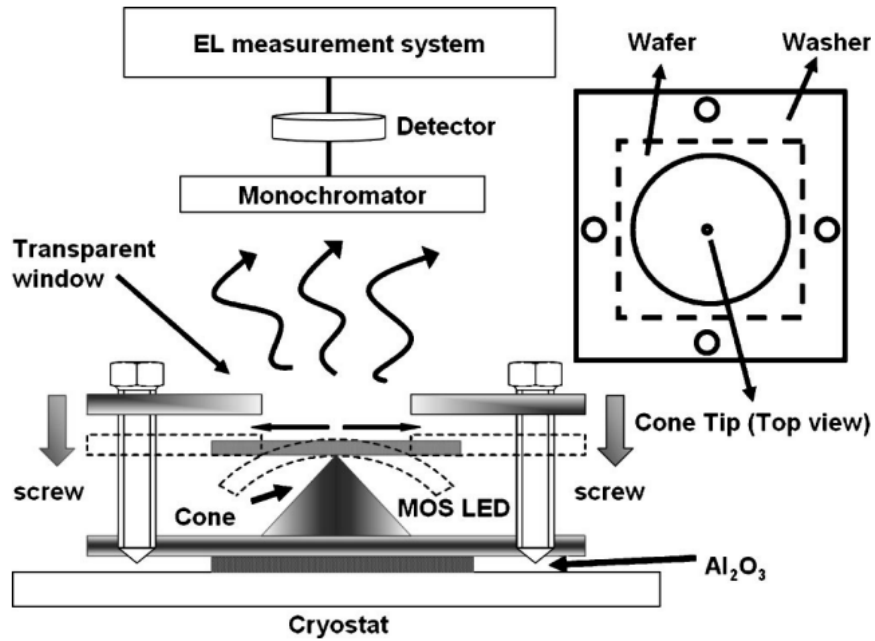


Figure 2.8 Schematic of mechanical bending setup. [56]

Therefore, other approaches to apply a larger tensile strain in Ge have been extensively investigated. Mechanical bending of a thick Ge substrate using the setup shown in Figure 2.8 has achieved 0.37% biaxial strain, resulting in a further enhancement of direct band gap recombination [24]. Another work on relatively thick (28 μm) membranes etched from bulk Ge has shown that tensile strain as large as 0.6% can be induced using a constant water pressure on the membrane [44]. Tensile strain as large as 2% in a very thin (20 nm) Ge layer on a polyimide film was

temporarily achieved using high-pressure gas as shown in Figure 2.9 [42], [57]. More than 2% tensile strain in Ge was demonstrated by growing a Ge layer on lattice relaxed InGaAs/GaAs buffer layers by molecular beam epitaxy (MBE) [58]. Other efforts include highly strained nanocrystal structures that show an increase by 2 orders of magnitude in photoluminescence as compared to bulk Ge [59].

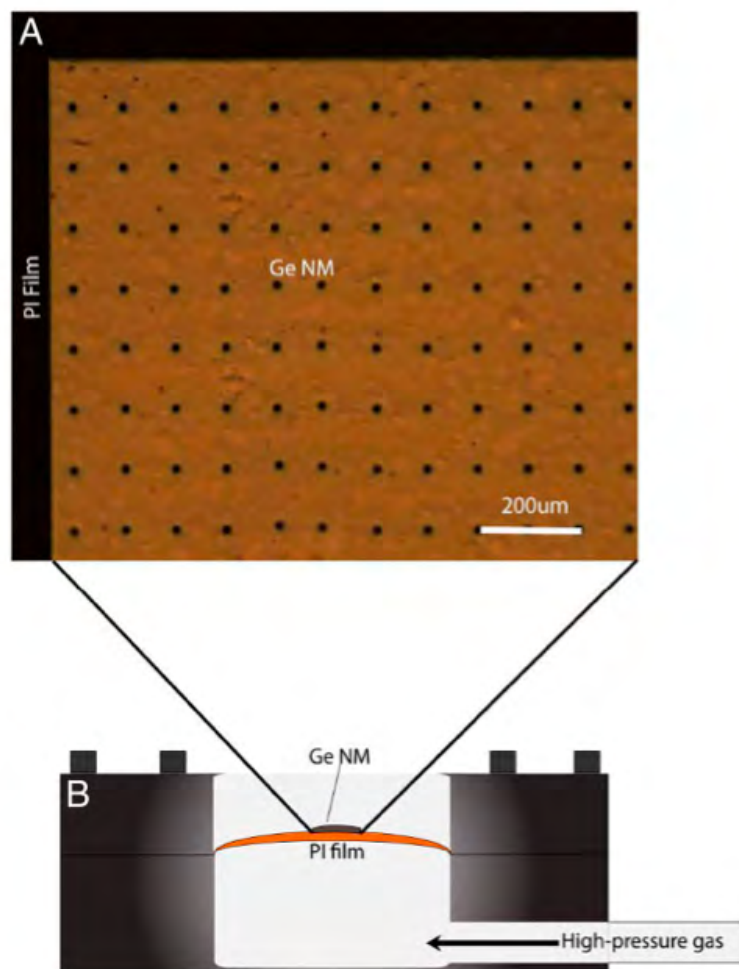


Figure 2.9 Strained Ge nanomembrane on a polyimide film. [42]

Although these works have experimentally verified the concept of improving the optical properties of Ge by strain, most of them are either impractical for device integration or associated with materials that are not fully CMOS-compatible. Therefore, in this dissertation, we will essentially put our effort in developing a new method for strained Ge which involves only CMOS-compatible materials and is fully practical for device integration.

Chapter 3

Biaxially Strained Ge Membrane

Integrated on a Si Substrate

3.1 Introduction

In this chapter, we present a technique to apply a sustainable biaxial tensile strain larger than 1% in a thin ($<2 \mu\text{m}$) Ge membrane integrated on a Si substrate. Raman spectroscopy confirms the amount of tensile strain in membranes and photoluminescence shows a large enhancement in light emission efficiency as well as a direct band gap reduction of nearly 100 meV. Simulation results using a tight-binding model [60], [61] predict that a combination of 1.1% tensile strain and 5×10^{19}

cm^{-3} n-type doping can reduce the required injection carriers for population inversion in Ge by nearly two orders of magnitude compared to an undoped and unstrained Ge. In order to show the possibility of device integration, vertical PN diodes are fabricated on these highly strained Ge membranes and photocurrent measurements show excellent responsivity well beyond $1.6 \mu\text{m}$ in strained PN diodes. We also demonstrate electroluminescence from PN diodes on highly strained Ge membranes. To investigate the implications of this membrane work, we propose a vertical-cavity surface-emitting laser (VCSEL) using a highly strained Ge membrane as a gain medium. Using finite-difference time domain (FDTD) simulations and a tight-binding band structure model, we predict that the threshold current density in a 1% strained VCSEL will be reduced by more than a factor of 3 compared to a 0.2% strained case.

3.2 Fabrication of Strained Ge Membrane

A high quality n-type Ge membrane of $1.6 \mu\text{m}$ thickness is fabricated using heteroepitaxial Ge growth on Si, in-situ doping and a selective etching process as depicted in Figure 3.1. First, a 500 nm thick SiO_2 layer is thermally grown on a double-side polished Si wafer. Windows of various sizes are then defined by optical lithography on one side and the wafer is dipped into 6:1 buffered oxide etch (BOE) for 7 minutes to create an etch mask of patterned SiO_2 . A $1.6 \mu\text{m}$ thick n-type Ge layer is then grown on the bare Si side using multiple hydrogen annealing for heteroepitaxy (MHAH) for a high-quality and smooth-surface [52]. When the wafer cools down after the final hydrogen annealing at 825°C , 0.2% tensile strain is accumulated due to the

large thermal expansion mismatch between n-type doped Ge and Si [50]. Then, an approximately 205 nm silicon nitride layer is deposited by plasma enhanced chemical vapor deposition (PECVD) as an anti-reflection coating in order to avoid Fabry-Perot modes in the thin Ge membrane. Using the patterned SiO₂ as an etch mask, Si is etched anisotropically from the backside in TMAH solution at 90 °C for approximately 6 hours [62]. After Si is etched all the way up to the top Ge layer, a 1.6 μm thick Ge membrane remains due to the high etch selectivity of Si over Ge in the TMAH solution. The membrane is still under 0.2% tensile strain since it is fixed at the edges and cannot relax. To further suppress Fabry-Perot modes, 80 nm of titanium was deposited on the backside by a magnetron sputtering system, since the germanium has a lower reflection coefficient to titanium. Then, to introduce a higher tensile strain in this membrane, tungsten is deposited on the backside at 4 mTorr pressure using a magnetron sputtering system. It is well known that the residual compressive stresses in tungsten can be larger than 4 Gpa by lowering the chamber pressure [63], [64]. As the compressive stressor tends to expand when it is released from a thick substrate, the membrane gets deflected and becomes tensile strained as shown in a scanning electron micrograph (SEM) (Figure 3.2 (a)) and a 3D image constructed via a white light optical interferometer (Figure 3.2 (b)).

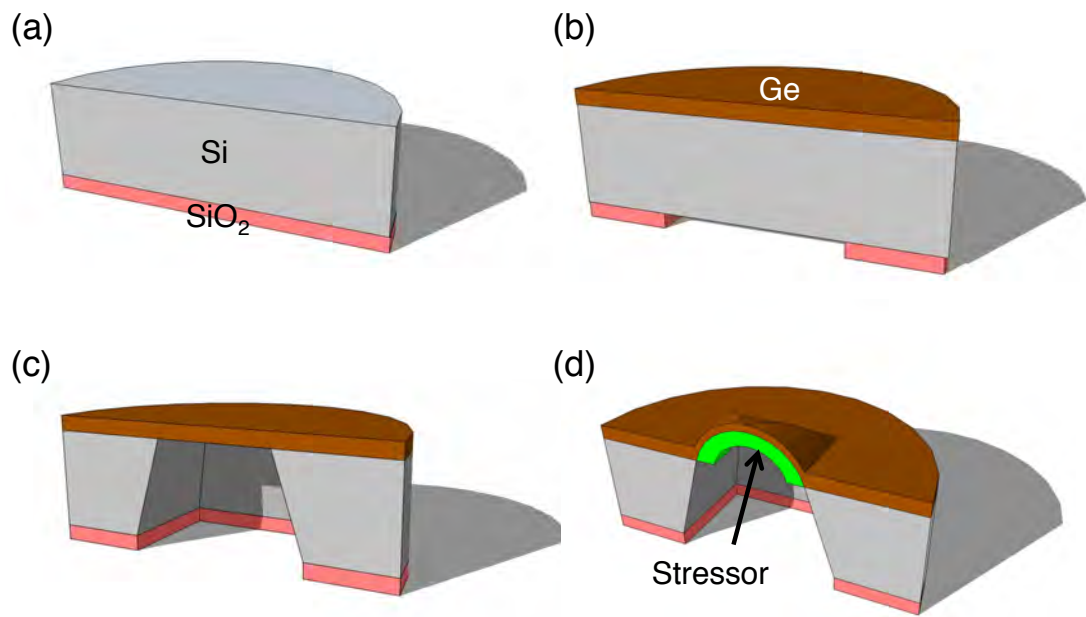
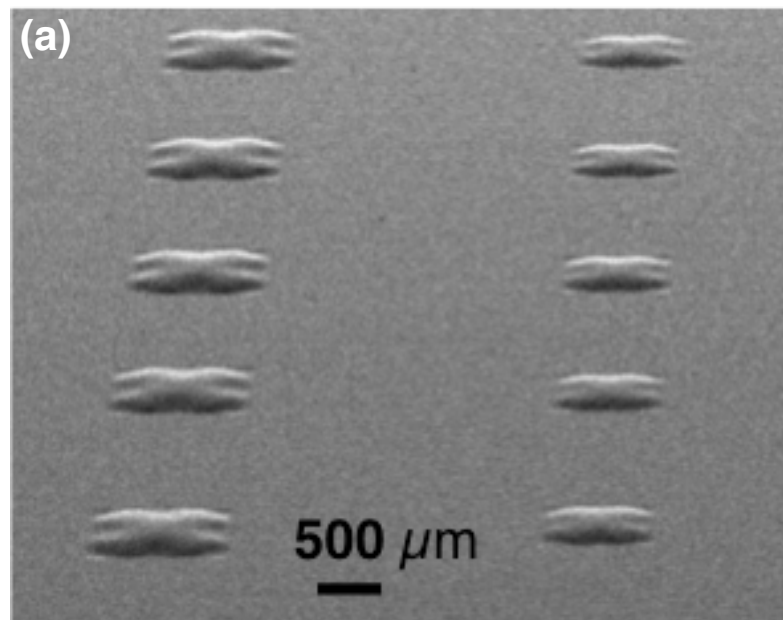


Figure 3.1 Fabrication process flow for highly strained Ge membranes



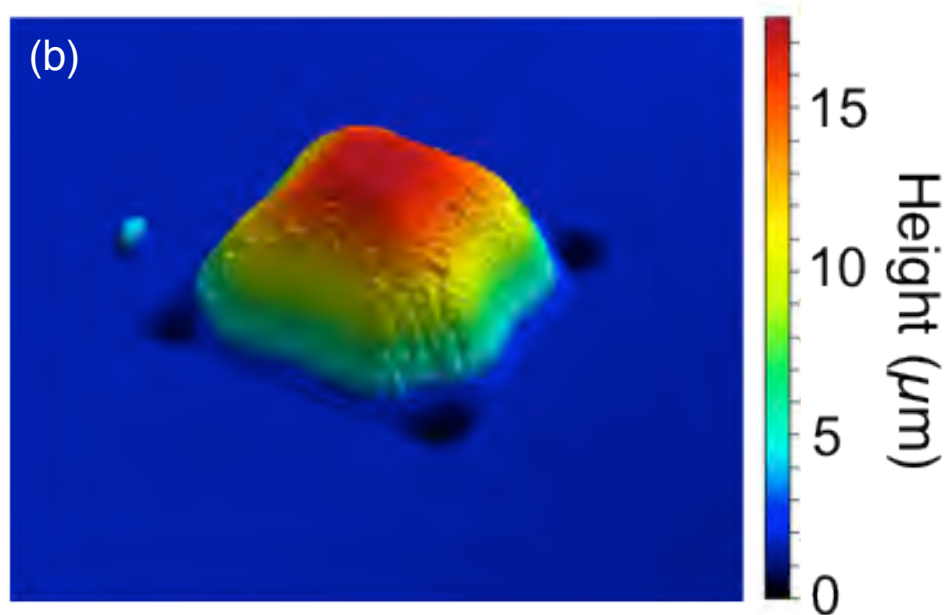


Figure 3.2 (a) SEM and (b) 3D profile of a strained Ge membrane.

3.3 Characterization of Strained Ge Membrane

A biaxial tensile strain larger than 1% was measured from both room temperature photoluminescence (PL) and Raman spectroscopy measurements. The excitation wavelengths were 532 nm and 514 nm for PL and Raman spectroscopy measurements, respectively. Both measurements were conducted at room temperature and the laser excitation power on the sample for PL was approximately 10 mW. A strained InGaAs detector cooled to -100°C by liquid nitrogen was used to perform the measurements over an extended wavelength range.

3.3.1 Mechanical Property Characterization

In Figure 3.3, Raman spectroscopy measurements show the amount of biaxial tensile strain in four different samples, crystalline Ge and Ge membranes with no stressor, 500 nm, and 900 nm tungsten stressor layers. Compared to crystalline Ge, the peak position shifts to the left as tensile strain is introduced in Ge membranes by thermal expansion mismatch for free standing membrane [50]. The peak shifts even further by depositing thicker stressor layers. According to the equation for strain calculation from Ref. [37], the samples with 500 nm and 900 nm tungsten are under $0.76\% \pm 0.10\%$ and $1.13\% \pm 0.13\%$ biaxial tensile strain, respectively, where the errors are due to the resolution limit of the setup.

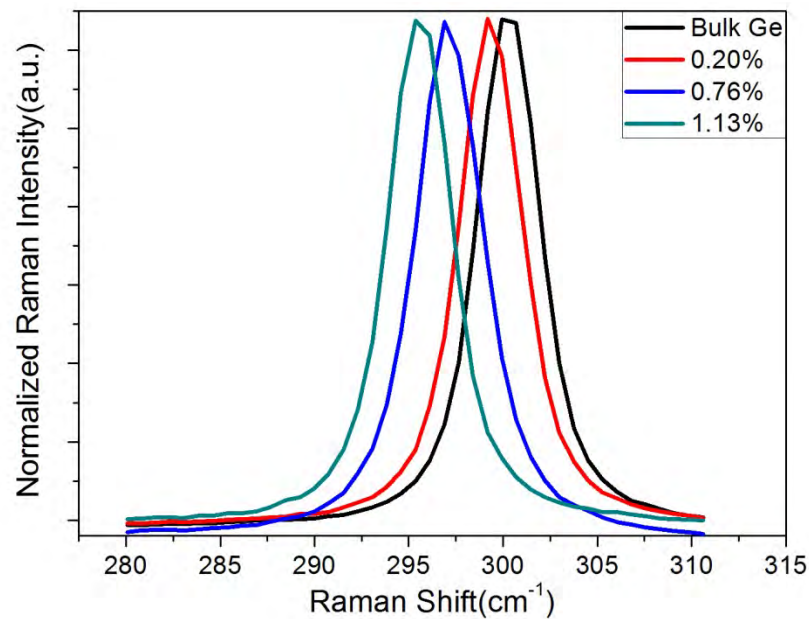


Figure 3.3 Normalized Raman spectra for membranes under various amounts of strain.

3.3.2 Optical Property Characterization

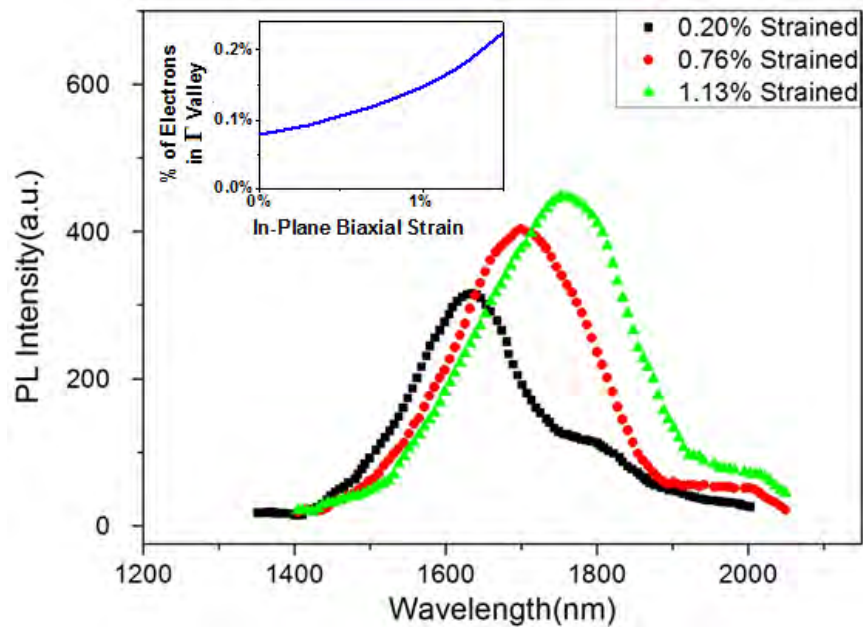


Figure 3.4 Room temperature PL spectra for membranes under various amounts of strain. The inset shows how the percentage of electrons in the Γ valley increases with strain according to our simulations.

PL measurements also confirmed a large tensile strain in our membrane as shown in Figure 3.4. The dominant peaks are due to the transition from the direct Γ valley to the heavy-hole band [42], [44]. Figure 3.4 shows the peak wavelengths of 1620 nm, 1690 nm and 1750 nm for a free standing and strained membranes, respectively. Moreover, the integrated PL intensity from the 1.13% strained membrane is approximately twice as large as from the 0.2% strained membrane. The inset of Figure 3.4 shows how the percentage of electrons in the Γ valley increases with strain, assuming heavy n-type doping. This is because higher strain lowers the direct Γ valley

edge relative to the indirect L valley edge, thereby increasing spillover from the indirect L valley into the direct Γ valley. Since the PL spectrum is dominated by transitions from the direct Γ valley, we expect the increase in gamma valley population to be roughly proportional to the integrated intensity of the PL signal. Comparing the 0.2% strained and 1.13% strained cases, our theoretical modeling of a 2x increase in Γ valley population is in good agreement with our experimental results which show approximately a 2x higher integrated PL intensity.

3.4 Theoretical Modeling for Population Inversion

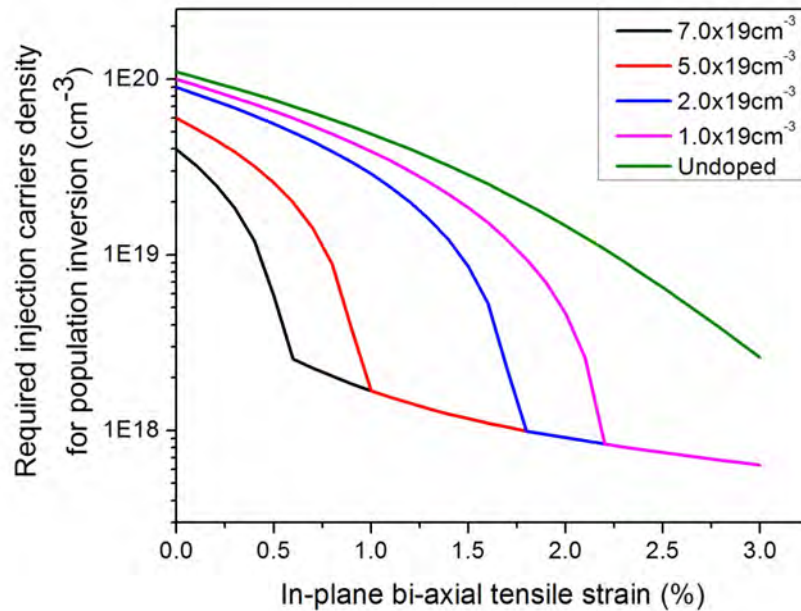


Figure 3.5 Required injection carrier density for population inversion versus strain for different n-type doping concentration.

Looking toward future lasing applications, population inversion in Ge is much more readily achievable with a combination of n-doping, which begins filling the indirect L valley, and strain, which lowers the direct Γ valley and also reduces the density of states in certain bands, notably the valence band. To quantify these changes, we have used sp³d⁵s* tight-binding with spin-orbital coupling [60], which incorporates diagonal parameter shifts due to the nearest-neighbor interactions when strain is present [61], to calculate the full band structure. From there, the carrier concentrations were approximated by summing the contributions from a mesh of evenly-spaced k-points over the entire first Brillouin zone. As shown in Figure 3.5, our simulations predict that a combination of strain and n-doping would drastically reduce the amount of pumping required for population inversion (i.e. electron quasi-Fermi level within the direct Γ valley, and hole quasi-Fermi level within the valence band). While an undoped and unstrained Ge membrane would require pumping of $1.1 \times 10^{20} \text{ cm}^{-3}$ to achieve population inversion, 1.1%-strained and $5 \times 10^{19} \text{ cm}^{-3}$ n-doped Ge requires pumping of only $1.6 \times 10^{18} \text{ cm}^{-3}$, a reduction of nearly two orders of magnitude. Note that the curves for n-doped Ge in Figure 3.5 saturate to a lower bound with increased strain; this represents the region where the electron quasi-Fermi level is already near or above the Γ -valley, and so the required pumping is determined by how many carriers are needed to push the hole quasi-Fermi level down to the top of the valence band. Since n-type dopant activation in Ge higher than $5 \times 10^{19} \text{ cm}^{-3}$ is readily achievable by either co-implantation of Sb and P [65] or laser annealing [66], our technique for larger than 1% strain strengthens the possibility of Ge laser for on-

chip interconnects. It should also be noted that our simulations predict a crossover of the direct band gap at roughly 2.2% strain, whereas most theoretical predictions claim the crossover occurs around 1.7-1.9% strain [16], [17], [32] and low-temperature PL experiments have suggested that 1.8% strain is already sufficient for a direct band gap at 5K [58]. In addition, there is some error introduced by approximating the carrier density by summing over a finite number of k-points. However, increasing the density (and accuracy) of the mesh of k-points tends to return slightly lower carrier densities in all valleys, which would increase the enhancement from n-doping. Thus, our simulations are likely understating both the enhancement from strain and the enhancement from n-type doping, and so these results should be viewed as conservative estimates.

3.5 Realization of Optoelectronic Devices

3.5.1 Integration of PN diodes on Strained Membranes

Vertical PN diodes were fabricated on highly strained membranes to show the possibility of device integration using our technique. Figure 3.6 shows a 3D schematic of a strained Ge PN photodetector. A 1.4 μm undoped Ge and a 250 nm n^+ -Ge layers are grown epitaxially on a Si substrate using diluted 1% phosphine in-situ doping without a subsequent annealing to avoid phosphorous dopant diffusion [52]. A 450 nm high Ge mesa is then patterned by dry etching, leaving p-type Ge as a supporting layer for a thin Ge membrane structure. Ti/Al metal contacts are realized by lift-off method

for both n- and p-type contacts. With a protective coating on the top surface, the Si substrate is etched and tungsten is deposited from the backside in order to introduce a higher strain. Figure 3.7 is an image from optical microscope showing a strained PN diode.

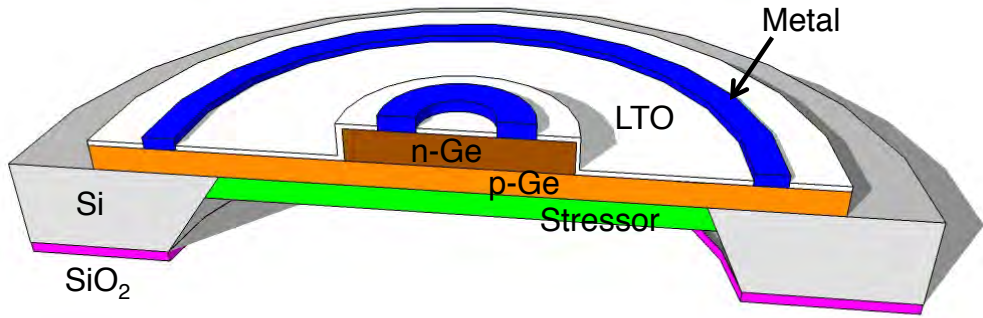


Figure 3.6 Schematic diagram of a strained Ge PN diode.

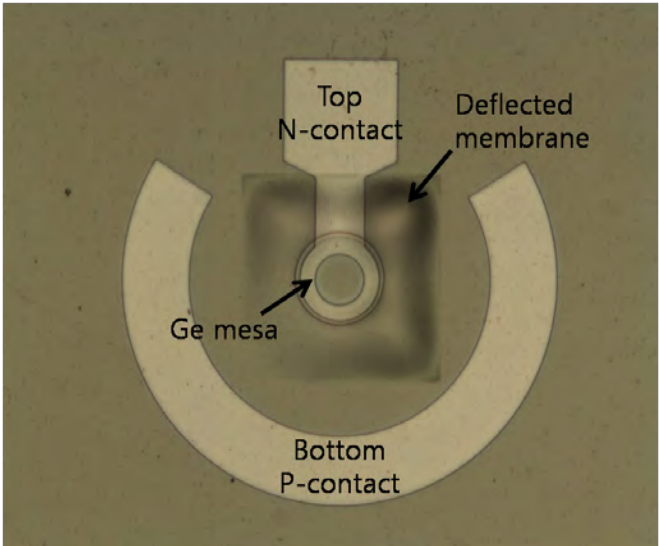


Figure 3.7 Optical image of a strained PN diode showing a deflected active region.

3.5.2 Current-Voltage Characteristics

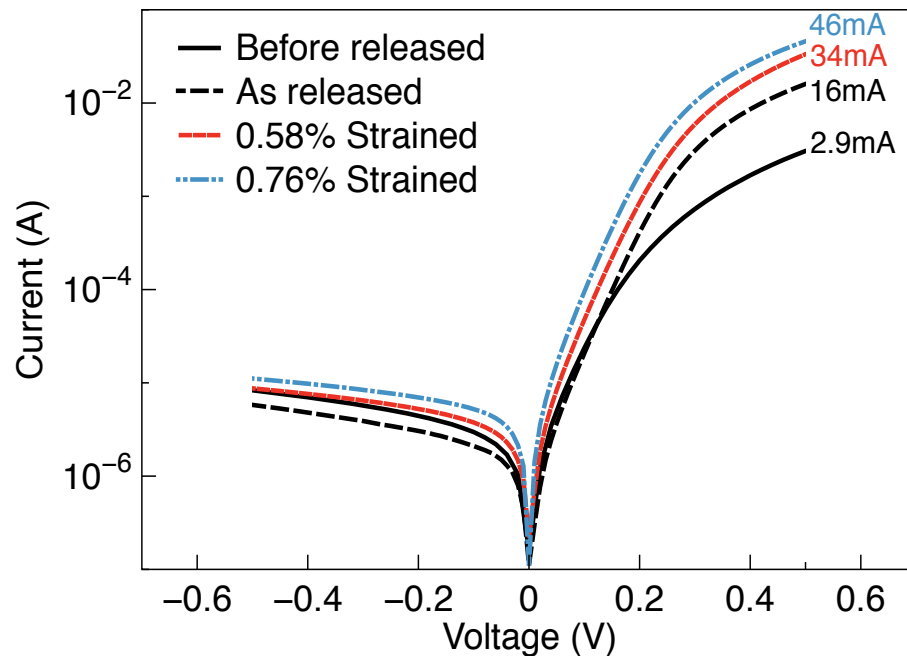


Figure 3.8 Current-voltage characteristics of PN diodes on several highly strained membranes. On-off ratio increases by one order of magnitude as Si is etched away. Strain further enhances both on and off current.

We performed electrical measurements at room temperature before and after etching away the Si. The solid black curve in Figure 3.8 shows the current-voltage (I-V) characteristic of a Ge PN diode on a Si substrate, showing an on-off ratio of approximately two orders of magnitude. After the Si is etched, the on-off ratio increases by one order of magnitude, as shown in the dotted black curve, due to a decrease in dark current and an increase in forward current. We believe that the dark current reduction is because etching the Si also removes some portion of the defective

region at Si/Ge interface, causing a decrease in the recombination current under reverse bias. Additionally, in the absence of Si, the tighter electric field distribution within the thin Ge layer may extend the depletion region closer to the p-type metal contact, resulting in a smaller series resistance, and this may explain why the forward current under the bias of 0.5 V increases almost by one order of magnitude. This forward current can be further enhanced with tensile strain because the band gap reduction increases the intrinsic carrier concentration, and possibly because electron mobility increases with tensile strain [16], [67]. Since strain can increase the fraction of electrons in the direct Γ valley, which has a smaller effective mass than the indirect L valley, the overall electron mobility increases with strain. Also, because of the increased number of holes in the light-hole band due to the strain induced heavy-hole / light-hole energy splitting, the effective hole mobility increases, too. While an as-released PN diode shows a forward current of 16 mA at 0.5 V, the forward currents in 0.58% strained and 0.76% strained PN diodes increase to 34 mA and 46 mA, respectively. The forward current enhancement will be much more prominent if we employ a P^+ -N diode where the hole current dominates because the hole mobility increases much faster than the electron mobility according to Ref. [37].

3.5.3 Photocurrent Measurement

The photocurrent measurement was conducted by shining light from a tunable optical parametric oscillator on the center of the mesa while the device was under 1 V bias. Figure 3.9 shows the normalized photocurrent spectra from three different

samples with 0.2%, 0.58%, and 0.76% biaxial tensile strain. The device with a 0.2% strained active region shows a roll-off of the measured photocurrent below 1.6 μm due to the direct band gap in Ge. Notably, diodes with both 0.58% and 0.76% bi-axial tensile strain show an excellent responsivity well beyond 1.6 μm . This effect can be attributed to the direct band gap reduction in Ge resulting in an enhanced absorption for longer wavelengths. Multiple peaks at around 1.55 μm and 1.7 μm are due to the Fabry-Perot cavity enhancement from the free-standing Ge membrane and the inset shows the calculated enhancement factor in the 1.65 μm Ge membrane PN diode using the transfer matrix method [68].

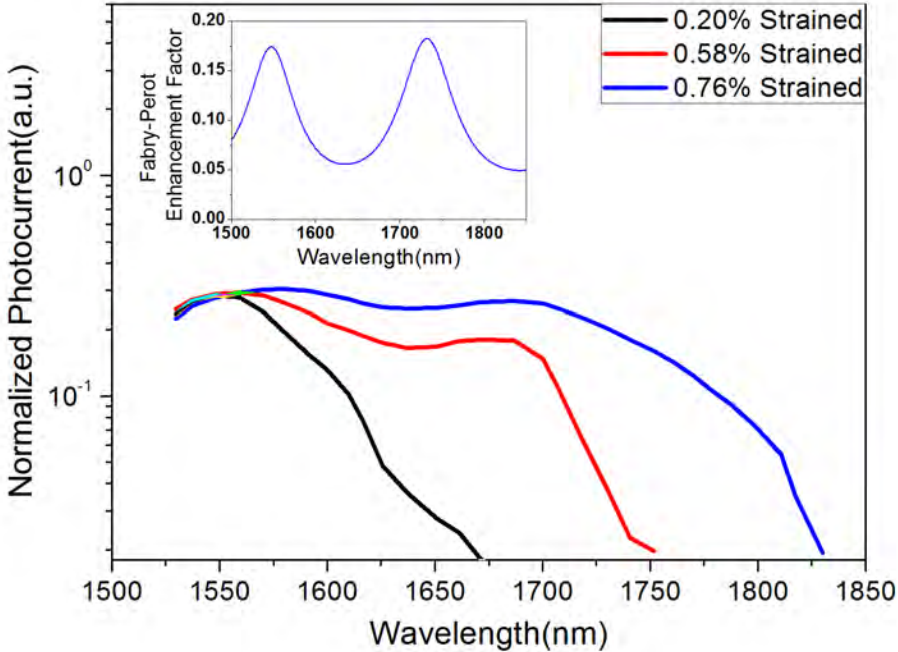


Figure 3.9 Normalized photocurrents from strained PN diodes. Inset shows the calculated Fabry-Perot enhancement factors in a 1.65 μm Ge membrane, assuming a complex refractive index of $n=4.35$, $k=0.01$.

3.5.4 Electroluminescence Measurement

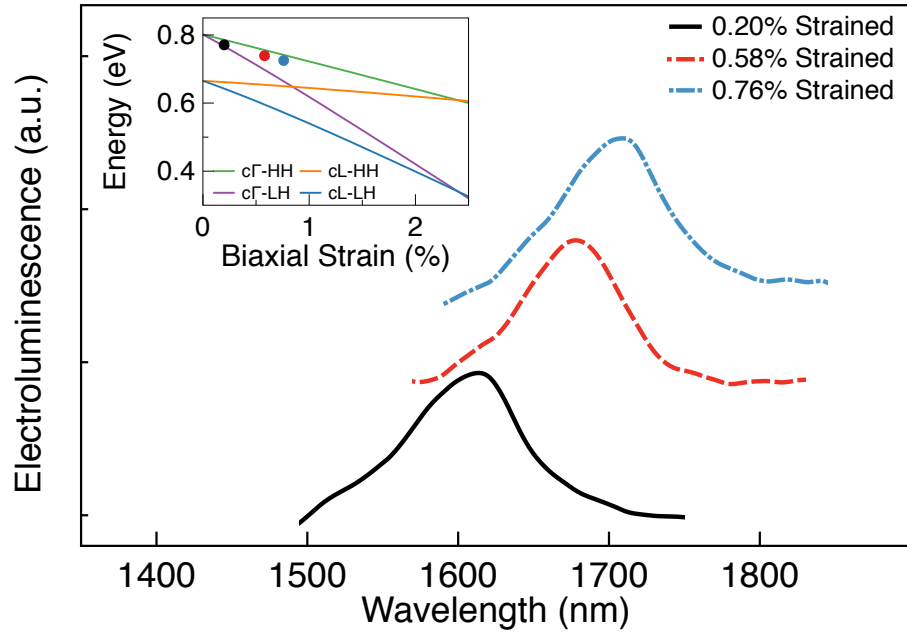


Figure 3.10 Normalized electroluminescence spectra. A 0.76% strained PN diode shows a 100 nm redshift of the center wavelength. The spectra are offset for clarity. The inset shows that the emission energies from these three samples are in good agreement with the calculated band gap energies.

We also performed electroluminescence (EL) measurements to show light emission from strained Ge membrane diodes. The measurements were conducted at room temperature at a current density of approximately 250 A/cm^2 . The emitted light was focused using a Mitutoyo 10x NIR objective lens with a numerical aperture (NA) of 0.26, and a strained InGaAs detector cooled to -100°C by liquid nitrogen was used to measure the signal over an extended wavelength range. As shown in Figure 3.10, an

as-released Ge diode emits a spectrum with a center wavelength of 1.6 μm , due to the 0.2% strain from thermal mismatch. By introducing tensile strains of 0.58% and 0.76% in the active region of PN diodes, we observed redshifts of the center wavelengths by 70 nm and 100 nm, respectively. These three spectra were normalized and the absolute EL intensities were not compared because the sample curvature in the highly strained LEDs can significantly affect the light extraction efficiency, especially with an objective lens of such a small NA. Fortunately however, with photoluminescence (PL) measurements the extraction efficiency is not significantly affected by the sample curvature, since the excited area of membrane is sufficiently small that it is approximately flat. By performing PL measurements, 30% and 50% efficiency improvements were observed in 0.58% and 0.76% strained samples, respectively, compared to the 0.2% strained case. The inset of Figure 9 shows that the emission energies from these three samples are in good agreement with the calculated band gap energies. When it comes to laser applications, strain effect on efficiency improvements will be much more significant than for LEDs because the optical net gain in a highly strained Ge is mainly contributed by the transition from the direct Γ valley to the light-hole band, and the smaller density of states (DOS) in the light-hole band facilitates population inversion, thus reducing the lasing threshold even further [25]. In the next section, therefore, we propose a laser structure on a highly strained Ge membrane and discuss the extent to which strain reduces lasing threshold.

3.6 Proposal for a Laser Structure

3.6.1 Optical Cavity Simulations

Figure 3.11(a) presents our proposed vertical-cavity surface-emitting laser (VCSEL) structure using a highly strained Ge membrane as the gain medium. This design can be easily integrated by replacing the Ge PN layer in our Ge PN diodes with a $p^+-Si_xGe_{1-x}/n-Ge/n^+-Si_xGe_{1-x}$ double heterojunction, and replacing the low temperature oxide (LTO) with quarter wavelength Si/SiO₂ distributed Bragg reflectors (DBR). In this structure, moderately doped n-type Ge (10^{18} cm^{-3}) sandwiched between SiGe layers serves as the laser's gain region. With the Si composition $x=0.15$ in SiGe layers, we expect most injected carriers to be confined in the Ge region due to the type I band offset of the SiGe/Ge/SiGe interface [10]. While the bottom DBR layer consists of three alternating quarter-wave Si/SiO₂ layers with reflectance $> 99\%$, the top DBR layer has only two alternating layers in order to preferentially emit light from the top surface. Using the transfer matrix method (TMM), the thicknesses of SiGe barriers and of Ge gain medium are carefully designed to support a cavity mode at the wavelength of highest optical net gain. To discuss the strain effect on the lasing threshold, we compared two cases: 0.2% and 1.0% tensile strain in the Ge gain medium. Resonant wavelengths were chosen to be 1515 nm and 1874 nm for 0.2% and 1.0% strain cases, respectively. The Ge thickness was set at 348 nm for 0.2% strain and 453 nm for 1.0% strain in order to have one full wavelength within the gain medium. Using FDTD simulations in Figure 3.11(b), it is shown that the optical mode can be tightly confined within SiGe/Ge/SiGe region due to the highly reflective DBRs.

We find Q-factors of 677 and 598 for the 0.2% and 1% strain cases, respectively, and optical losses for the two cases are calculated to be 262 cm^{-1} and 235 cm^{-1} , respectively. In order to achieve lasing in these structures, net modal gain (material gain divided by optical confinement factor) should exceed the optical loss from the cavity. With an optical confinement factor of approximately 0.3 in both cases that is calculated from TMM, the threshold gain coefficients for two cases are 873 cm^{-1} and 783 cm^{-1} .

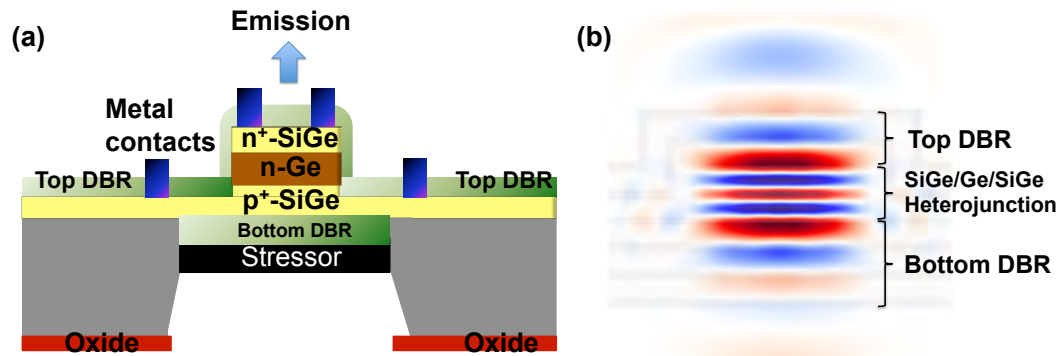


Figure 3.11 Proposal of a laser structure. (a) Proposed VCSEL structure using a highly strained Ge as a gain medium. (b) FDTD simulations show that the optical mode can be tightly confined in the heterostructure.

3.6.2 Lasing Threshold Calculation

Using $sp^3d^5s^*$ tight-binding with spin-orbital coupling and diagonal parameter shifts from nearest-neighbor displacements [60], [61] to calculate the band structure of strained Ge, and extrapolating the presumed absorption coefficients of Ref. [25] to

higher strains, we obtained optical net gain spectra as a function of injection current density for both 0.2% and 1% strained Ge gain media cases as shown in Figure 3.12(a). Our theoretical calculations of threshold current account for all the major forms of recombination: radiative recombination from the Γ valley, radiative recombination from the L valley, non-radiative Shockley-Reid-Hall recombination, and non-radiative Auger recombination [25]. Since the intervalley scattering rate is much faster than all of these interband recombination mechanisms [69], we can simply take the L and Γ valley electron populations to be in exact equilibrium with each other with a single shared quasi-Fermi level. Because tensile strain lowers the direct Γ valley faster than the indirect L valley, and also because biaxial tensile strain reduces the density of states (DOS) at the top of the valence band by light-hole / heavy-hole splitting, we find that increasing the strain from 0.2% to 1.0% reduces the required current density for positive optical net gain from 256 kA/cm² to 43 kA/cm². For our proposed structure, moving from 0.2% to 1% strain in the gain media reduces the threshold current density for lasing from 503 kA/cm² to 151 kA/cm². Particularly for room temperature laser operation, the reduction of threshold current density has a significant meaning because high currents can lead to serious heating problems, which may adversely affect laser operation. The black curve in Figure 3.12(b) shows the projection of threshold current density vs. strain up to 2% in a moderately n-type doped Ge (10¹⁸ cm⁻³) gain medium, assumed threshold gain coefficient of 1000 cm⁻¹ is required to overcome cavity losses. Note that the net gain of 1000 cm⁻¹ is not a fundamental upper limit, but rather just the threshold gain for this one particular cavity

design. Net gains of several thousand cm^{-1} are theoretically possible before the gain saturates due to free carrier loss at much higher currents. While 1% strain reduces the threshold by approximately one order of magnitude compared to the unstrained case, pushing the strain up to 2% for the direct band gap Ge is expected to reduce the threshold current density by a factor of 1000 compared to the unstrained case. Since the wavelength of highest net gain would be red-shifted beyond $2\ \mu\text{m}$ as shown in the red curve in Figure 3.12(b), our tunable strained membrane technique can also be utilized for highly efficient mid-infrared laser applications.

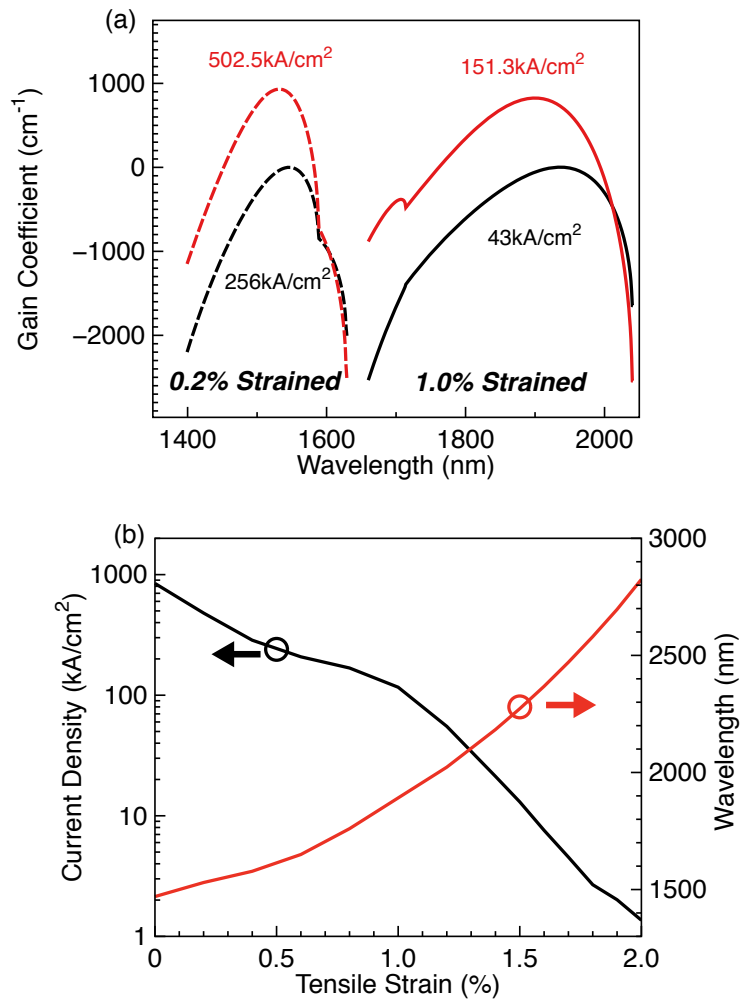


Figure 3.12 Theoretical modeling for a low-threshold Ge VCSEL. (a) Gain spectra for 0.2% and 1% strained Ge cases, showing a 1% strained case reduces the threshold current density more than a factor of three compared to a 0.2% case. (b) Threshold current density and the wavelength of highest optical net gain versus strain.

3.7 Conclusion

We have proposed and demonstrated a method to fabricate a thin Ge membrane integrated on a Si substrate and induce a sustainable and large tensile strain by depositing a stressor layer to improve the Ge's optical properties. From room temperature photoluminescence and Raman spectroscopy measurement, larger than 1% biaxial tensile strain is confirmed in highly strained membranes and a direct band gap energy reduction of 100 meV is observed. Light emission efficiency from the 1.13% strained membrane was significantly improved compared to the 0.2% strained membrane, as predicted in our simulation for the fraction of electrons in the Γ valley versus strain. According to our tight-binding calculations, population inversion in 1% strained and heavily doped Ge can be achieved with two orders of magnitude less injection than unstrained and undoped Ge. Moreover, we presented the first device fabrication using highly strained Ge and showed an excellent responsivity well beyond 1.6 μm from a 0.76% strained Ge PN diode. We also demonstrated electroluminescence from these highly strained PN diodes. A 0.76% strained diode showed a 100 nm redshift in the spectrum and improved I-V characteristics. Finally we proposed a VCSEL using a highly strained Ge membrane as a gain medium. Using

FDTD simulations and a band structure model, we exhibited the possibility of an efficient Ge laser. We believe that our strain-tunable membrane can ultimately be utilized for high efficiency near-infrared lasers, which are essential to realize on-chip optical interconnects.

Chapter 4

Uniaxially Strained Ge Wires via CMOS-Compatible Approach

4.1 Introduction

In the previous chapter, we showed the feasibility of a highly strained Ge membrane as an efficient light-emitting material. Although the membrane technique enabled the creation of the first optoelectronic device integrated on highly strained Ge membranes, this approach of etching a Si substrate to create a Ge membrane may be sometimes undesirable from a practical point of view because the Si etching process may be too time-consuming and make the Si wafer fragile.

In this chapter, therefore, we present a radically simple and fully CMOS-compatible approach to apply a large uniaxial tensile strain to Ge using geometrical amplification of a small pre-existing biaxial tensile strain [70]–[72]. We start this chapter with a discussion on the fabrication of a Ge-on-Insulator (GOI) wafer which will be used for our new approach. This GOI wafer not only provides a high-quality Ge film with a reduced defect density compared to the Ge film on Si [73], but also allows us to obtain a Ge membrane structure much more easily without etching the Si substrate because of the presence of the sacrificial oxide layer underneath the Ge layer. Then we present the working principle of the geometrical amplification of strain. Next, we discuss several types of PL measurement results for a detailed study of carrier dynamics in highly strained Ge wires. We finally conclude with a discussion of the implication of these uniaxially strained Ge wires towards an efficient Ge laser.

4.2 Ge-on-Insulator Wafer Fabrication

Over the past decade, epitaxial growth of Ge on Si has made significant progress. By hydrogen annealing at high temperature, researchers significantly minimized the propagation of the defects that are inevitably created at the interface between Si and Ge due to the large lattice mismatch [51]–[53]. Therefore, as shown in a cross-sectional transmission electron microscope (TEM) image (Figure 4.1), the top surface of the epitaxial Ge film can be of high quality and there have been many research reports on successful demonstration of electronic devices such as metal-oxide semiconductor field-effect transistor (MOSFET) fabricated on this Ge platform [51],

[74]. However, unlike MOSFET for which the carriers are transported only at the high-quality top surface, the performance of optical devices may be hampered by the defects at the bottom of the Ge layer. For example, the injected carriers into Ge via optical/electrical pumping should be quickly redistributed over the whole Ge layer and the defects at the bottom of the Ge layer may serve as non-radiative recombination centers, thereby reducing the light emission efficiency [75]. Therefore, it is desirable to eliminate the defects if one desires to realize an efficient Ge light source.

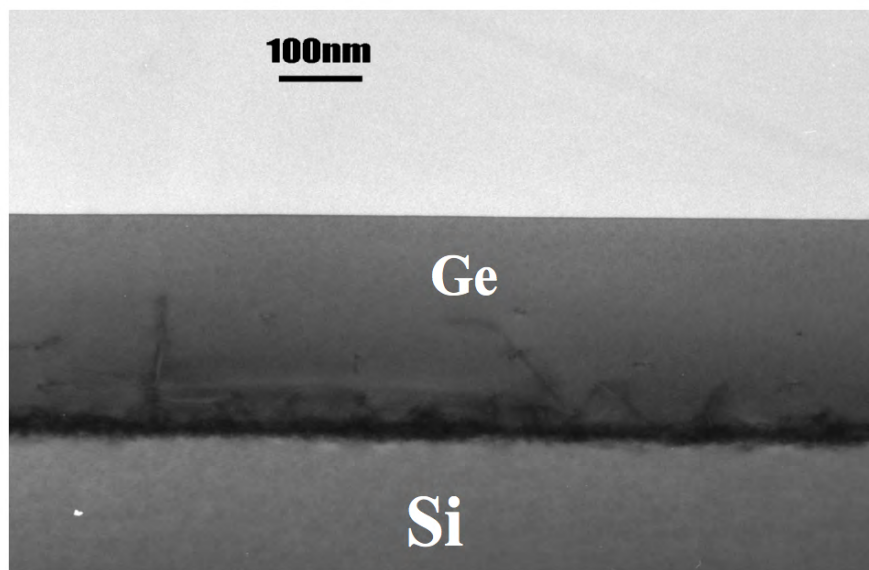


Figure 4.1 Cross-sectional TEM image of epitaxially grown Ge film on Si. [53]

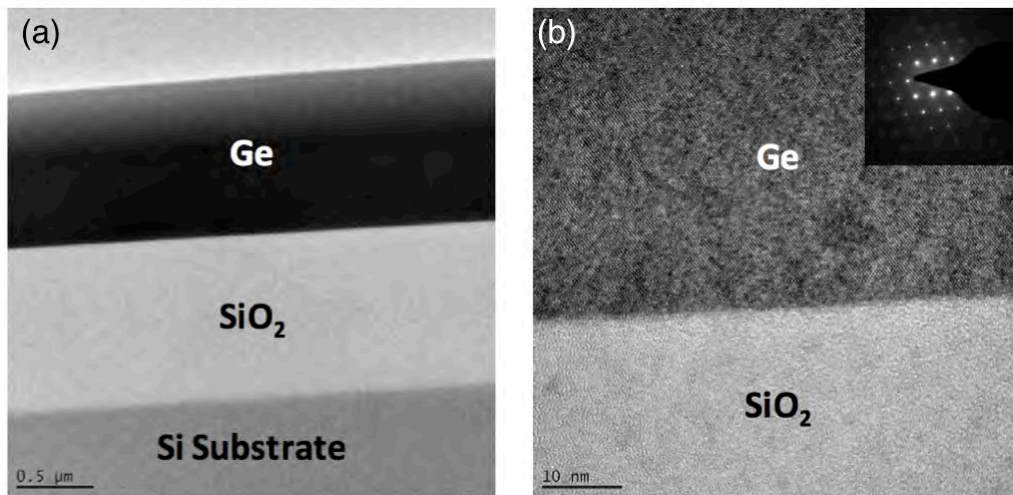


Figure 4.2 Cross-sectional TEM images of GeOI. [73]

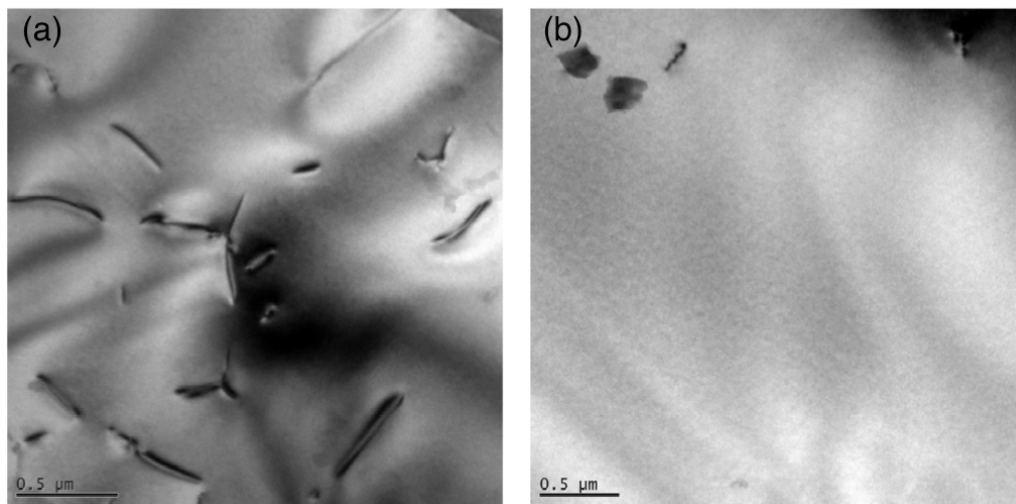


Figure 4.3 Plan-view TEM images of Ge film before and after CMP processing. [73]

Recently, researchers presented methods to fabricate Ge-On-Insulator (GOI) wafers by layer transfer techniques [73], [76], [77]. By transferring the epitaxial Ge film to a handle wafer and by removing the defective region via chemical-mechanical

polishing (CMP), a high-quality Ge film on insulator was obtained as shown in cross-sectional TEM images (Figure 4.2). As evidenced by the plan-view TEM images of the Ge film before (Figure 4.3(a)) and after (Figure 4.3(b)) the CMP processing, the defect density in the final Ge film can be significantly reduced.

Following a similar process step of Ref. [73], a GOI wafer was fabricated to obtain a high-quality Ge film with a reduced defect density compared to the Ge film on Si, as depicted in Figure 4.4. To begin, a ~ 2 μm thick Ge layer was epitaxially grown on a Si substrate using the multiple hydrogen annealing heteroepitaxy (MHAH) technique followed by wafer bonding to an oxidized Si wafer. After bonding, the bonded wafer was annealed at 300 °C for 3 hours in order to enhance the bonding force between Ge and oxide layers. After the post-bond anneal, the Si substrate of the carrier wafer is etched in TMAH solution at 90 °C to obtain a GOI wafer. The hydrogen annealing technique eliminates most defects and dislocations away from the Ge-Si interface of the carrier wafer, and the wafer bonding flips the Ge, leaving most of the remaining defects close to the top surface of the GOI wafer. A biaxial tensile strain of $\sim 0.2\%$ is accumulated during the growth due to the different thermal expansion coefficients between Si and Ge, and this strain remains after wafer bonding [73]. A high-quality single-crystalline Ge layer is then obtained by thinning the Ge layer to 500 nm with a wet etch using aluminum etchant, thereby eliminating the remaining defects at the top surface. It is worth noting that the presence of the oxide layer underneath Ge will be particularly useful in creating a membrane structure. In

the next chapter, we will discuss a new method to create a large tensile strain in Ge from the GOI wafer.

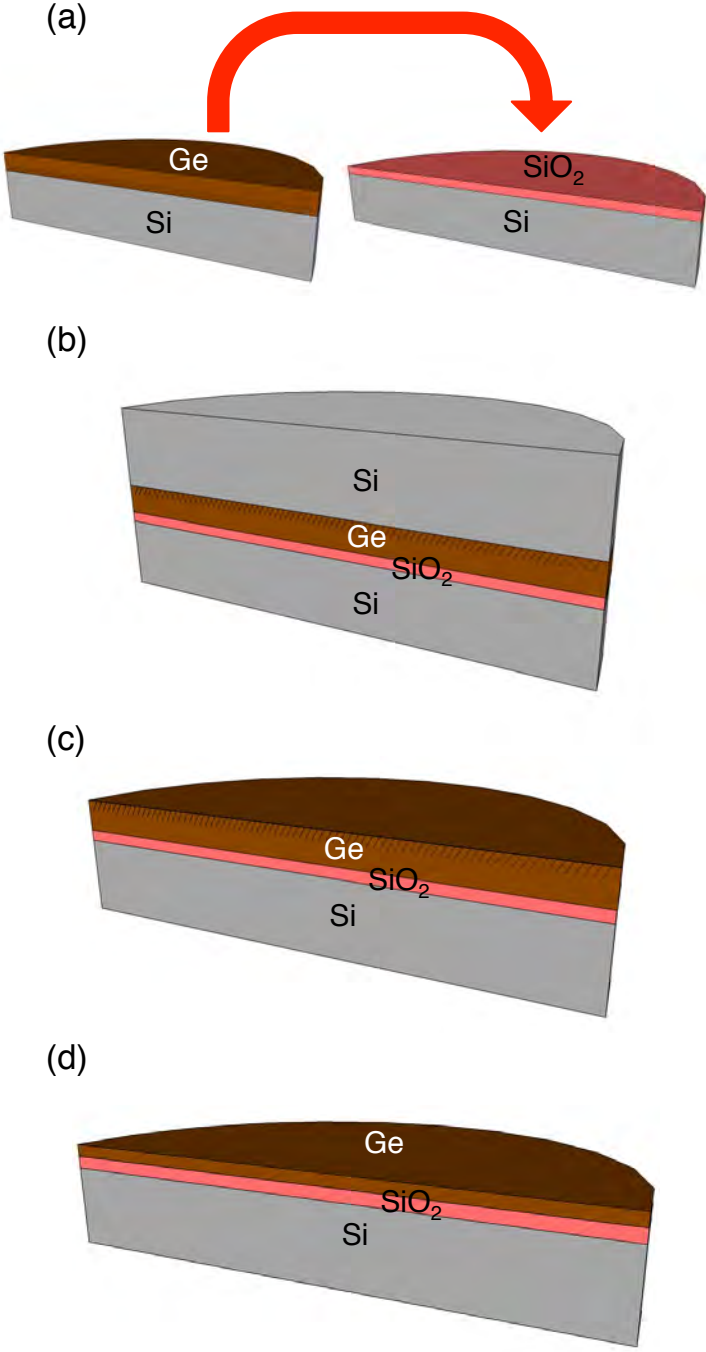


Figure 4.4 Process flow for GOI wafer fabrication.

4.3 Creation of Uniaxially Strained Ge Wires

4.3.1 Working Principle of Geometrical Amplification of Strain

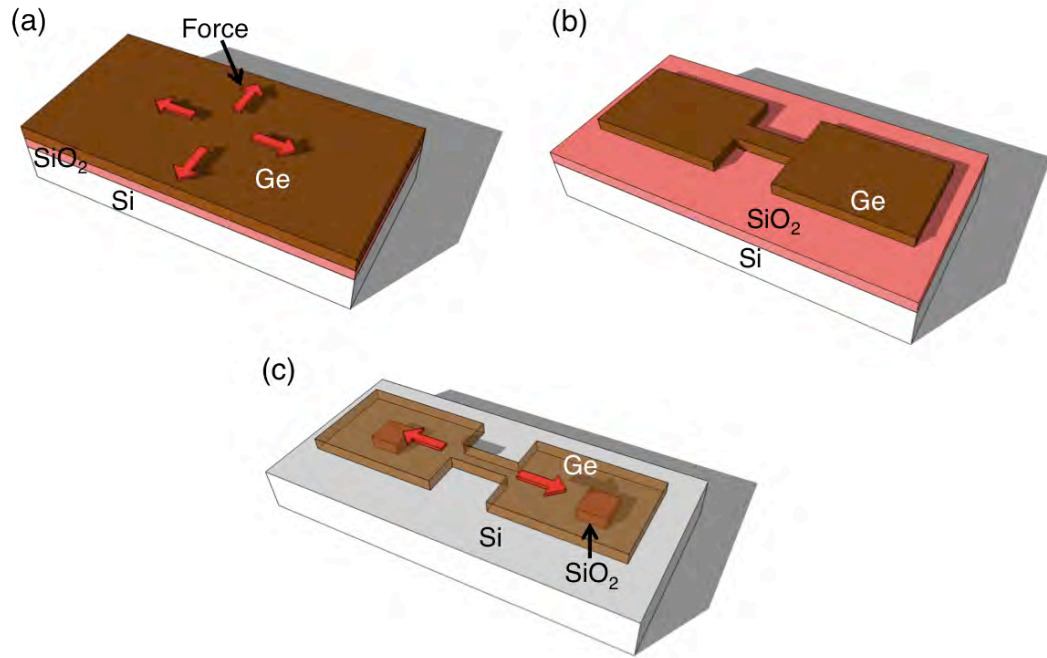


Figure 4.5 Fabrication process flow for uniaxially strained Ge wires.

Recently, Minamisawa et al. demonstrated a large tensile strain in Si nanowires up to 4.5% using the strain accumulation mechanisms [70]. Extending upon this strain concentration technique onto our GOI wafers with 0.2% strain in the Ge layer, we created localized uniaxial strains greater than 1.5% in the Ge wires. The fabrication process is depicted in Figure 4.5. Starting from a GOI wafer with 0.2% biaxial strain as shown in Figure 4.5(a), the top Ge layer is patterned using electron-beam

lithography to form a narrow wire connecting two wide pads as shown in Figure 4.5(b). HF vapor etch is used to remove the sacrificial oxide layer in order to release the Ge layer. When the patterned Ge layer with pre-existing 0.2% biaxial tensile strain is suspended by etching the sacrificial dielectric underneath, the strain in the transverse direction is relaxed everywhere, while an interesting phenomenon occurs for the remaining longitudinal uniaxial strain. Along this axis, the barrier regions relax, shrink in size, and pull apart the central Ge wire. This causes significant uniaxial strain concentration in the narrower wire because the force per area at the two ends of the central Ge wire is significantly increased due to the reduced cross section of the wire [70]. By changing the length and the width of the two wide pads with fixed wire geometry, various degrees of uniaxial strain along the [100] direction can be selectively induced in the Ge wires. After the wire is fully strained by completely etching away the underlying oxide layer, the top Ge layer was intentionally adhered to the Si substrate by using capillary force associated with the surface tension of water [78]. This adhesion process has a negligible impact on the strain distribution throughout the structure, and the large uniaxial strain in the micro-bridge is entirely preserved. Bringing the top Ge layer down to Si significantly improves the thermal conductivity in the Ge wire by creating a path for heat conduction towards the thick Si substrate.

Figure 4.6(a) shows an SEM image of a fully fabricated Ge wire under a large uniaxial strain. In this experiment, the width and the length of the central wires are fixed to 6 μm and 18 μm , respectively, and strain in the wire is controlled by changing

the length of the large pad regions. Finite-element method (FEM) COMSOL simulations were performed to predict the strain distribution within the wire as shown in Figure 4.6(b). Figure 4.6(c) shows an optical micrograph of a typical sample under investigation, including the excitation laser spot size using a 100x magnification objective lens. Within the optical excitation area, the strain distribution is almost uniform according to FEM COMSOL simulations as shown in Figure 4.6(d).

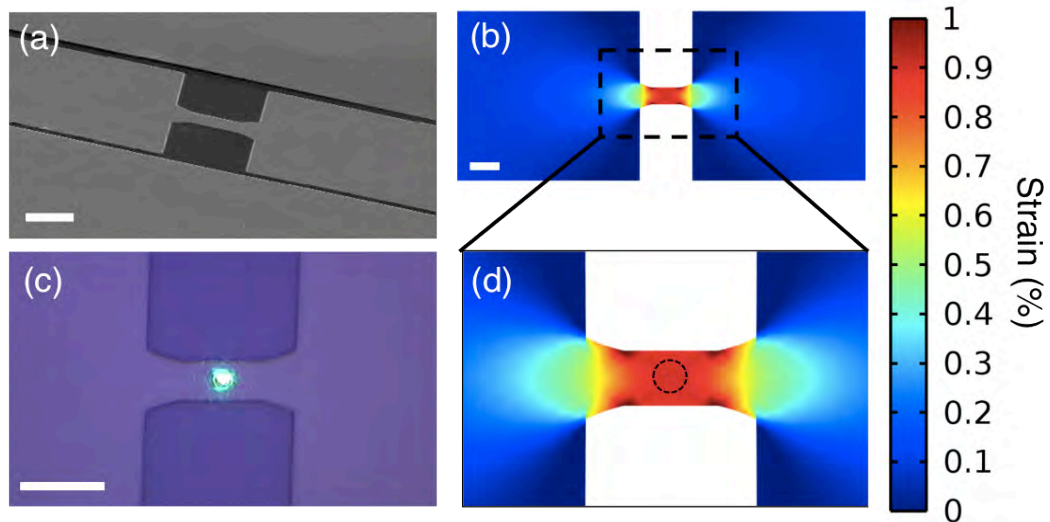


Figure 4.6 SEM images and simulation results of uniaxially strained Ge wires. (a) SEM image of a fabricated Ge wire. Scale bar, 10 μm . (b) Finite-element COMSOL simulation of the structure. Scale bar, 10 μm . (c) Optical micrograph showing an excitation laser spot. Scale bar, 10 μm . (d) A zoomed-in image of Figure 4.6(b) showing a uniform strain distribution within an area of the laser spot size.

4.3.2 Strain and Band Structures

To measure the amount of uniaxial strain in a Ge wire on Si, Raman spectroscopy was performed using a WITEC Raman system. A 100x magnification objective lens was used to focus the 514nm-wavelength laser excitation within an area where the strain distribution is uniform as shown in Figure 4.6(b). Figure 4.7(a) shows Raman shift spectra measured from Ge wires with large pads of different lengths ranging from 10 μm to 500 μm . Each spectrum was fitted to a Lorentzian function and the relative shift of the spectra from bulk Ge was then calculated to obtain the strain level [72], [79], [80]. The increasing spectrum shift towards a longer wavelength (a smaller cm^{-1} value) as the pad length increases clearly indicates that the strain in the wire can be amplified in a controllable manner. Figure 4.7(b) shows schematic diagrams of unstrained and uniaxially strained Ge band structures. As shown in the diagrams, uniaxial strain reduces an energy separation between the direct and indirect conduction valleys and also causes a splitting of two degenerate valence bands (VBs). With uniaxial strain, the top valence band (VB) has a large effective mass along the strain axis and a small effective mass along the other two axes, giving it a relatively small DOS overall. The shape of the band structure becomes opposite for the second VB, which has a small effective mass along the strain axis, and a large effective mass along the other two axes, giving it a relatively large DOS overall. In the following section, we will study how the carrier dynamics is influenced by these changes in the band structure of a strained Ge using polarization-, temperature- and excitation-dependent PL measurements.

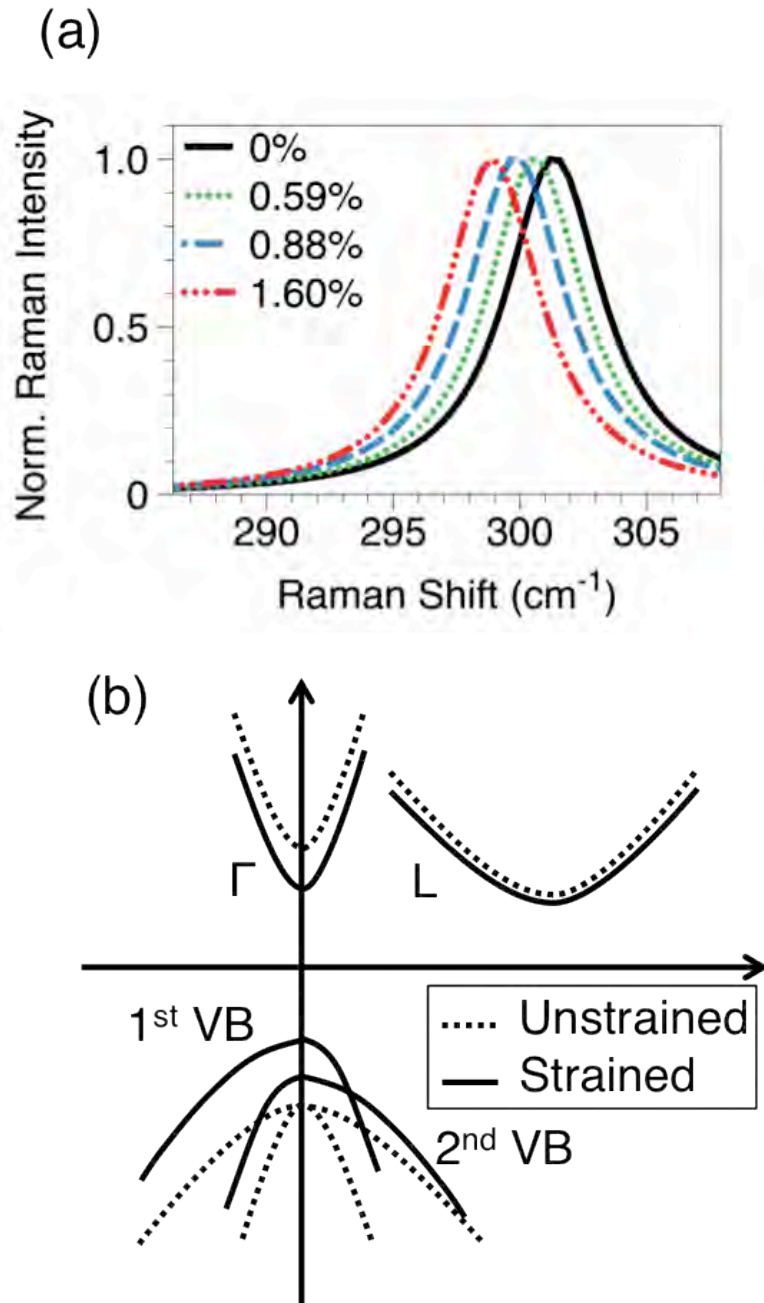


Figure 4.7 Raman measurements and Schematic of band structures. (a) Measured Raman spectra showing red-shifts with strain. (b) Schematic diagrams of band structures of unstrained and strained Ge in dotted and solid curves, respectively.

4.4 Carrier Dynamics Study

4.4.1 Strain-Dependent PL Measurement

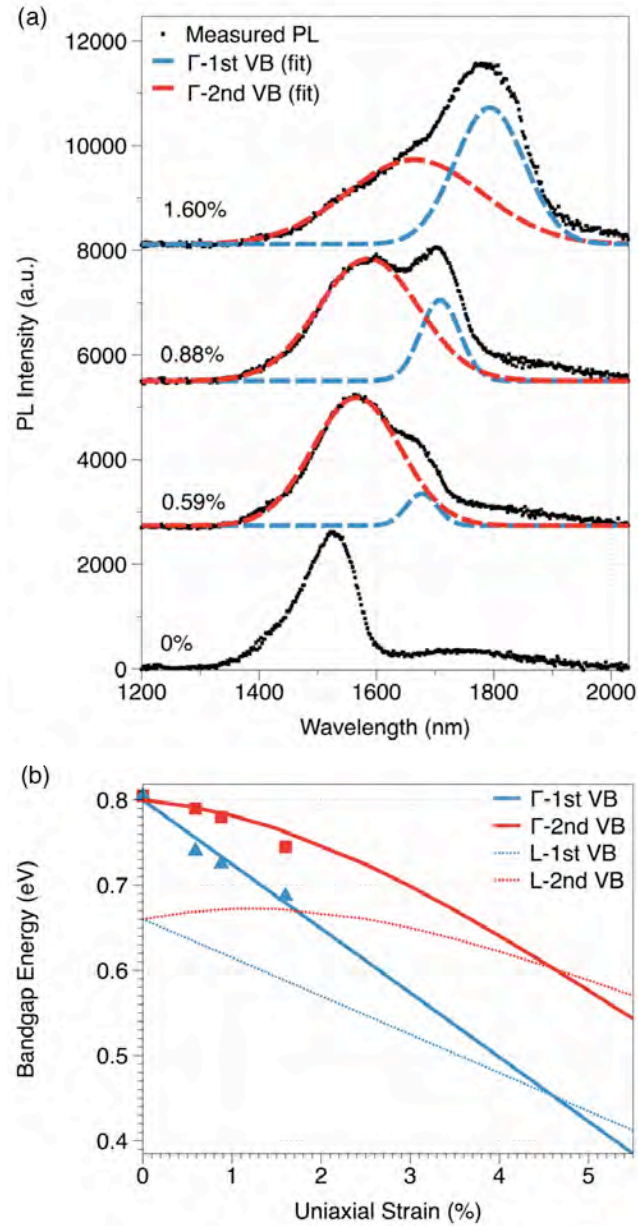


Figure 4.8 Strain-dependent PL measurement. (a) PL emission spectra from Ge wires with different strain levels (black). The blue dashed and red solid curves show the

fitted Gaussians for each of the two different optical transitions. (b) Calculated band gap energies shown in solid and dotted curves and the experimentally measured peak energies in squares and triangles.

Figure 4.8(a) shows typical PL spectra from Ge wires under different amounts of uniaxial strain. The optical excitation with a 532 nm-wavelength laser was tightly focused onto the center of wires using a 100x objective lens. The integrated excitation power for Figure 4.8 was ~ 20 mW. While such a high power quickly causes heating problems in any suspended sample [81], this was not the case for our samples with post-release stiction as evidenced by a constant PL peak position under various excitation conditions, i.e. the absence of band gap narrowing [82]. The curves with black squares are experimentally measured PL spectra. As shown in the bottom curve of Figure 4.8(a), unstrained Ge shows a PL peak located at ~ 1.55 μm which originates from an optical transition between the Γ valley and the two degenerate VBs. Another weak emission is observed at a longer wavelength around 1.8 μm and arises from a transition between the indirect L valley and the two degenerate VBs. As the uniaxial strain is increased to 0.59%, not only is the peak position of the direct band gap transition shifted to a longer wavelength, but also there seems to be a second peak at an even longer wavelength. As strain is further increased to 0.88% and 1.60%, two peaks continue to shift to longer wavelengths and the second peak becomes more pronounced as shown in the upper two curves. By fitting multiple Gaussians to the measured PL curves, the two peaks are clearly resolved and shown as solid and dashed

curves. The blue (red) curves at longer (shorter) wavelengths are from the optical transitions between the Γ valley and the 1st (2nd) VB as shown in Figure 4.7(b). The peak positions of the two separate optical transitions due to strain-induced valence band splitting are compared to simulated band gap energies as a function of strain using deformation potential theory as shown in Figure 4.8(b) [17]. The blue (red) curve represents the theoretical band gap energies for the Γ -1st VB (Γ -2nd VB) separations. Band gap energies for the L-1st VB (L-2nd VB) are also presented to show the reduced energy band gap separation between the direct and the indirect transitions with higher strain. Red squares and blue triangles representing the experimental peak positions are in good agreement with the theoretical band gap energies.

4.4.2 Polarization-Dependent PL Measurement

To further prove that the two peaks arise from strain-induced valence band splitting, we performed polarization-dependent PL measurements as shown in Figure 4.9. The black curves represent PL spectra collected without a polarizer. The red (blue) curves show PL spectra collected with a polarizer aligned perpendicular (parallel) to strain axis. PL spectra from unstrained Ge shown in the bottom curves reveal that polarization of emitted photons is insignificant because two PL spectra with a polarizer aligned along two different directions are almost the same. As shown in the upper curves, however, the emitted photons from strained Ge wires are strongly polarized since the red and the blue curves show a significant difference. It is clearly

noticeable that the emission at a longer wavelength which comes from the Γ -1st VB transition is strongly polarized perpendicular to strain axis. A similar observation was made by Pollak and Cardona in [83] where the effect of uniaxial compression on the electroreflectance peaks of Ge was studied. It has been shown that for compressive strain along the [100] direction, the PL intensity associated with the 2nd VB should be strongly polarized perpendicular to strain axis. Tensile strain reverses the order of two VBs and the 2nd VB in case of compressive strain becomes the top-most VB in our case. This explains the observed dominance of perpendicular polarization of the emitted photons from the Γ -1st VB transition.

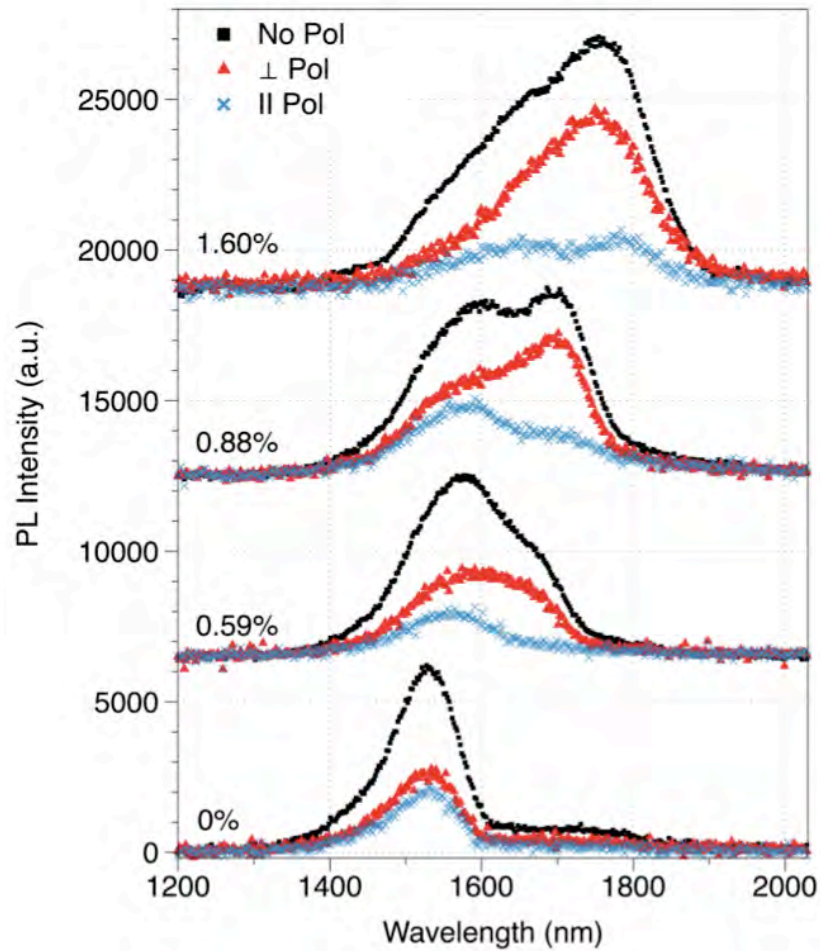


Figure 4.9 Polarization-dependent PL measurement. The black curves are PL spectra collected without a polarizer. The red (blue) curves are spectra collected with a polarizer perpendicular (parallel) to strain axis.

4.4.3 Temperature-Dependent PL Measurement

We also performed temperature-dependent PL measurements to study how electrons and holes populate different bands at various temperatures. Figure 4.10 shows three different PL spectra from a 0.88%-strained Ge micro-bridge in black, red and blue for measurements conducted at room temperature, -50 °C and -100 °C, respectively. Among the two peaks associated with each of the two VBs, the left peak at a shorter wavelength is from the Γ -2nd VB transition and has a higher peak intensity than the other at room temperature. At -50 °C, however, the right peak at a longer wavelength from the Γ -1st VB transition has higher peak intensity than the peak from the Γ -2nd VB transition. This means that holes are more likely to populate the 1st VB than the 2nd VB at lower temperature. This phenomenon can be attributed to the reduced thermal energy which increases the percentage of holes in the uppermost VB due to the reduced tail of the Fermi-Dirac distribution. As the reduced thermal energy at lower temperature also decreases the electron population in the higher Γ valley for analogous reasons, the integrated PL intensity becomes smaller at lower temperature as shown in the three curves. The integrated PL intensity is further reduced at -100 °C while the left peak associated with the 2nd VB becomes almost

invisible, meaning that the hole population in the 2nd VB is further reduced. Another peak at $\sim 1.8 \mu\text{m}$ comes from the indirect band gap transition and its intensity does not change significantly at lower temperature because the change in the electron population in the L valley is negligible. The peak locations also consistently shift to shorter wavelengths as temperature is decreased due to the effect of temperature on the band gap [82].

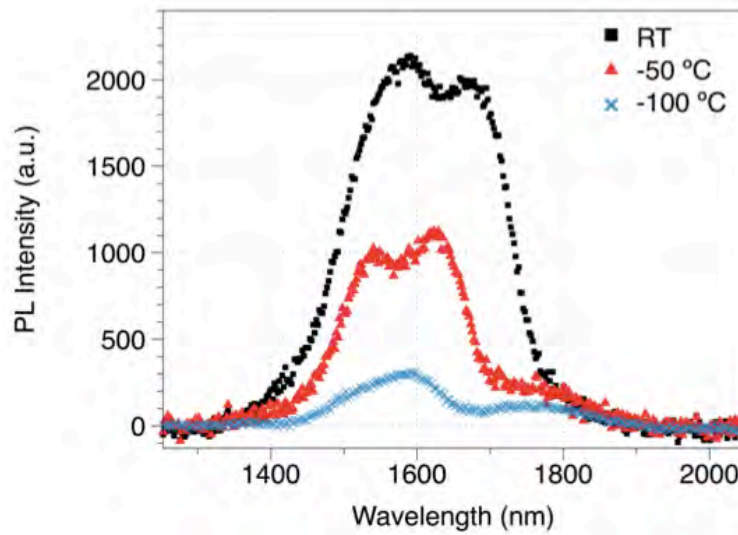


Figure 4.10 Temperature-dependent PL measurement.

4.4.4 Excitation-Dependent PL Measurement

In addition, excitation-dependent PL measurements were conducted to further investigate the carrier dynamics in strained Ge wires under different pumping conditions. Figure 4.11 shows the PL spectra from Ge wires with various amounts of strains under excitation powers of 2 mW, 15 mW and 30 mW. The PL spectra for 2 mW and 15 mW were accumulated for 20x and 2x, respectively, during the data

acquisition. By fitting multiple Gaussians to the spectra shown in Figure 4.11, we were able to conduct quantitative analyses on the electron and hole carrier dynamics in strained Ge wires as shown in Figure 4.12. Figure 4.12(a) shows the integrated PL intensities from strained Ge wires normalized to the emission intensity from an unstrained Ge wire. As strain increases the fraction of electrons in the Γ valley, the amount of radiative recombination from the direct band gap transition increases proportionally. Assuming Maxwell-Boltzmann statistics, i.e. assuming an electron quasi-Fermi level below the conduction band edge, every 1% strain is expected to increase the total PL emission by a factor of ~ 3.2 as shown in the theoretical enhancement curve in green [71], [72]. The PL enhancement at 2 mW (red) was $\sim 2.5x$ for every 1% strain and the slight discrepancy from simulation may be because strain increases the fraction of the photons that propagate preferentially along the in-plane direction of the micro-bridge and therefore cannot be detected in our setup where only photons emitted towards the top surface can be collected [42]. The enhancements at 15 mW (blue) and 30 mW (black) become noticeably smaller than the enhancement at 2 mW. This is because at higher excitation powers the Maxwell-Boltzmann assumption is no longer valid because the electron quasi-Fermi level is located within the conduction band. In this case, the occupancy probability is no longer exponentially dependent upon the energy of the conduction valleys, and so any change in the band structure results in a less substantial change to the overall carrier distribution. Figure 4.12(b) shows the integrated PL intensity ratio of the Γ -1st VB transition to the Γ -2nd VB transition at different excitation powers. At all pumping conditions, strain

significantly increases the fraction of the emission associated with the 1st VB which means the holes are more likely to populate the 1st VB with strain. Therefore, these two analyses clearly highlight the advantages of applying strain to Ge for a low-threshold laser because, with high strain, stimulated emission should occur due to Γ -1st VB transition as will be explained in the next section.

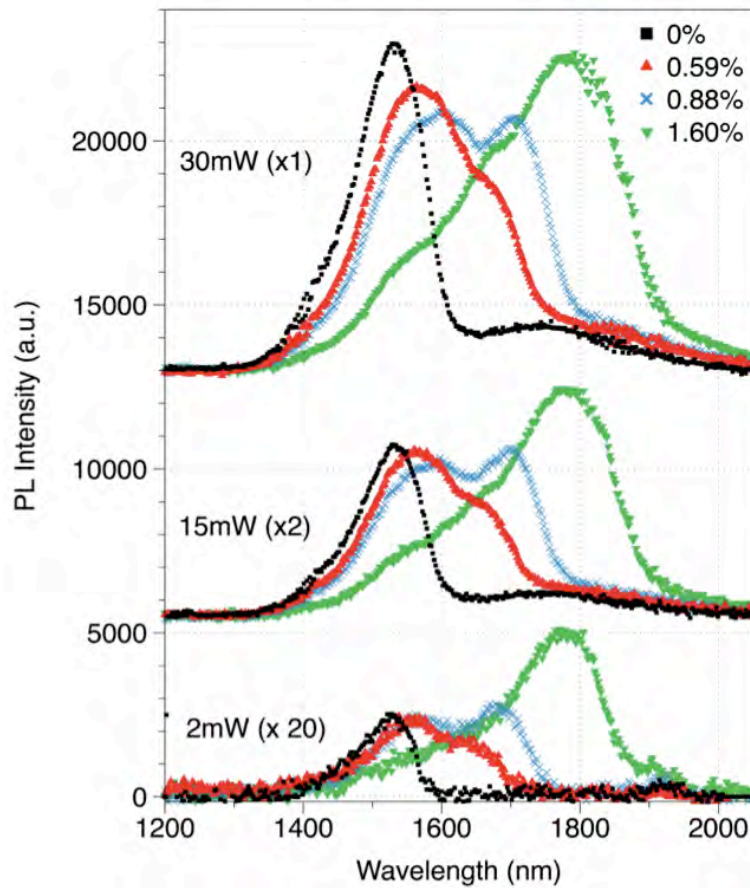


Figure 4.11 Excitation-dependent PL measurement. PL emission spectra from Ge wires with different strain levels, collected with excitation powers of 2 mW (bottom), 15 mW(middle) and 30 mW (top). The spectra with the 2 mW (15 mW) excitation were accumulated for 20x (2x).

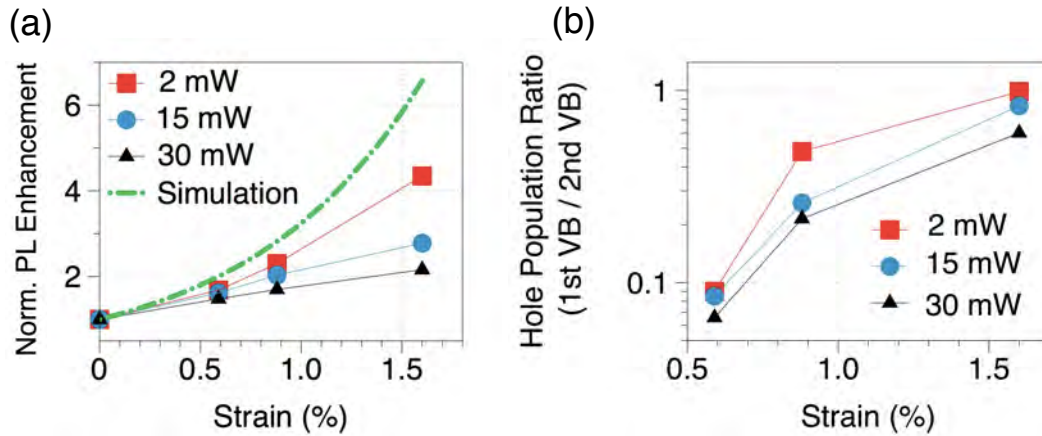
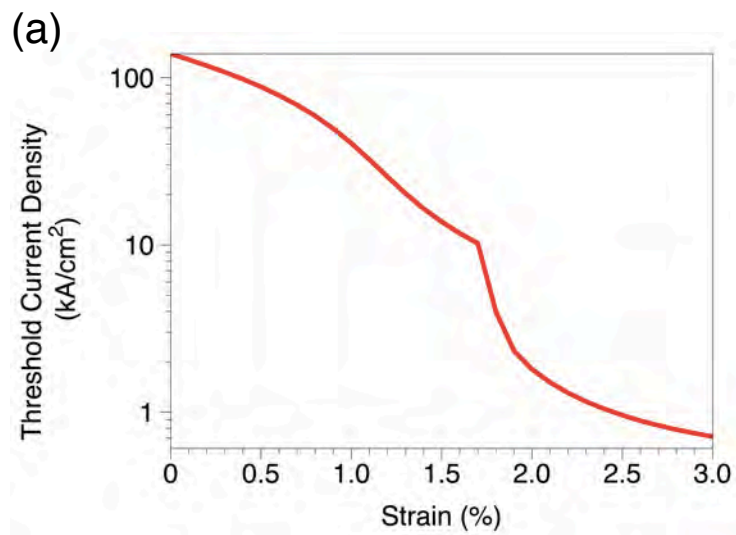


Figure 4.12 Quantitative study of carrier dynamics. (a) Strain-induced PL enhancement normalized to the emission from unstrained Ge at different excitation powers. (b) Integrated PL emission ratio of the Γ -1st VB transition to the Γ -2nd VB transition.

4.5 Theoretical Modeling for a Low-Threshold Ge Laser

Figure 4.13(a) shows how the lasing threshold of a Ge laser can be drastically reduced with uniaxial strain based upon theoretical modeling. This modeling assumes an ideal lossless optical cavity with 300nm-thick Ge with $5 \times 10^{19} \text{ cm}^{-3}$ n-type doping as the gain medium, and also assumes that lasing will always occur at the wavelength of peak net gain [41]. The doping value of $5 \times 10^{19} \text{ cm}^{-3}$ was chosen because it was the doping used in the initial Ge laser demonstration [54]. As strain increases the electron population in the Γ valley, the amount of pumping required for population inversion between the Γ valley and the valence bands decreases exponentially. At low strain levels, net optical gain is associated with the Γ -2nd VB transition as shown for 1%-

strained Ge with $4 \times 10^{19} \text{ cm}^{-3}$ carrier injection in the red dashed curve of Figure 4.13(b). Although population inversion is always achievable across the Γ -1st VB transition, at low strains it is not strong enough to overcome free carrier losses without additional contributions from the Γ -2nd VB transition with its larger DOS. Beyond a certain amount of strain, however, the valence band splitting increases enough that the Γ -1st VB transition alone can overcome free carrier absorption and starts contributing net optical gain, as shown for 2.5%-strained Ge with $5 \times 10^{18} \text{ cm}^{-3}$ carrier injection in the solid black curve of Figure 4.13(b). In this case, the population inversion occurs without pumping too many holes into the 2nd VB. Given the smaller DOS in the 1st VB, lasing off of the Γ -1st VB transition is thus expected to further reduce the lasing threshold. The kink in Figure 4.13(a) comes from this sudden switch from lasing with primarily the Γ -2nd VB transition to lasing with only the Γ -1st VB transition.



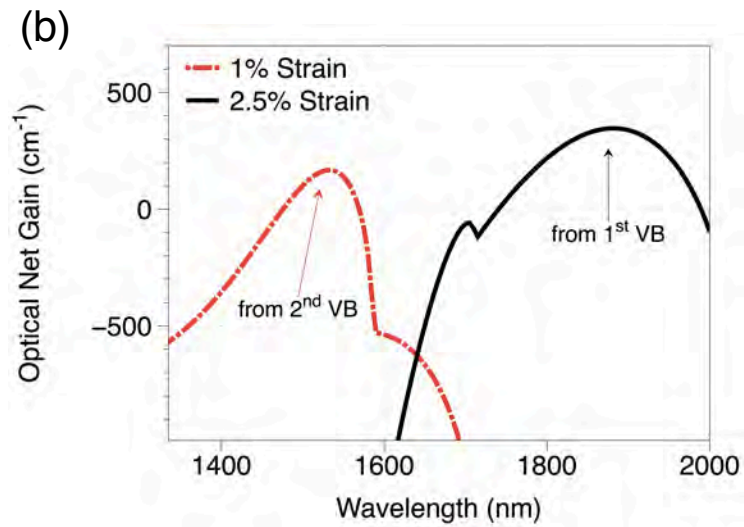


Figure 4.13 Theoretical modeling for a laser with uniaxially strained Ge as a gain medium. (a) Threshold current density vs. strain curve showing the decreased lasing threshold with strain, assuming 300nm-thick Ge with $5 \times 10^{19} \text{ cm}^{-3}$ n-type doping. (b) Net optical gain spectra for 1%- and 2.5%-strained Ge in red dashed and black solid curves, respectively. The respective carrier injection levels were $4 \times 10^{19} \text{ cm}^{-3}$ and $5 \times 10^{18} \text{ cm}^{-3}$, and the doping was held constant at $5 \times 10^{19} \text{ cm}^{-3}$.

4.6 Conclusion

We presented a CMOS-compatible approach to apply a large uniaxial tensile strain to Ge using geometrical amplification of a small pre-existing biaxial tensile strain. The GOI wafer with a high-quality Ge film allowed us to induce a localized strain in a Ge wire by removing the thin sacrificial oxide layer. Then, we investigated how uniaxial strain changes the band structure of Ge by experimentally observing

carrier dynamics through polarization-, temperature- and excitation-dependent PL measurements. The presence of two direct band gap transitions due to strain-induced valence band splitting was verified by a strong polarization of emitted photons and by the changes in the hole population between two VBs at various temperature conditions. The excitation-dependent PL measurements revealed that strain increases the electron population in the Γ valley and the hole population in the 1st VB, and we presented theoretical modeling of how these improved carrier dynamics in strained Ge can reduce the threshold of a Ge laser by $>100x$. We believe that these experimental observations along with the theoretical modeling will help pave the way towards an efficient Ge light source for optical interconnects.

Chapter 5

Strain-Induced Pseudo-Heterostructure with Tunable Band Profiles

5.1 Introduction

Since their introduction over half a century ago, semiconductor heterostructures have revolutionized electronic and photonic devices, in particular diode lasers [84]–[89]. Using a so-called “double heterostructure” wherein a narrow band gap region is sandwiched between two wide band gap regions, carriers can readily be confined in the narrow band gap region. This carrier confinement is especially vital to efficient laser operation [90], [91]. Until now, however, room temperature heterostructure

behavior was only achievable by stacking layers of different semiconductor materials together with substantial band offsets. For example, band offsets well in excess of the thermal energy kT at room temperature (~ 26 meV) are required to confine or trap carriers. Heteroepitaxy is costly due to the associated chemical vapor deposition (CVD) or molecular beam epitaxy (MBE) processes, and often further complicated by large lattice mismatches and/or incompatible thermal budgets for different semiconductors [92]. Moreover, since a different process step is required for each new material, only a small number of unique heterojunctions can be fabricated on a single wafer. All of these problems can be avoided if one can create heterostructures within a single material by locally modifying the material's band gap. Strain engineering is a well-established technique to modify the electronic band gap of virtually all semiconductors [16]. The lattice constant of a crystalline semiconductor increases with tensile strain, thereby reducing its electronic band gap [93]. Previously, researchers have shown spatial band gap modulation by mechanically bending nanostructures [94]–[96] and by depositing stressor layers [97], [98]. However, these methods have thus far been limited by either practicality or design flexibility for realizing heterostructure behavior within a single material, and no meaningful optical or electronic functions were experimentally demonstrated at room temperature.

In this chapter, we present the first experimental observation of room temperature carrier confinement within germanium (Ge) nanowires by creating strain-induced potential wells via the strain concentration technique introduced in the previous chapter. By tuning the strain profiles within Ge nanowires, custom-designed electronic

band profiles at the nanoscale were realized and arbitrary heterostructure profiles within nanowires of a single material were created. This single-material nanowire with full heterostructure behavior is termed pseudo-heterostructure in this work. Effective carrier collection within each strain-induced potential well increases the local carrier concentration significantly in an ultra-compact area, resulting in spatially-confined and enhanced light emission. The emission wavelength is also redshifted due the local band gap reduction in the tensile-strained nanowires. In this chapter, we demonstrate the spatially-confined (Figure 5.5), enhanced (Fig 5.7(a)), and red-shifted (Inset to Figure 5.7(a)) emission and quantitatively compare these results to our theoretical model.

5.2 Creation of Strain-Induced Potential Wells

Figure 5.1(a) shows a scanning electron micrograph (SEM) of a typical pseudo-heterostructure nanowire. It was realized by extending upon a strain concentration technique used for Si nanowires [70], which allowed us to induce localized strains greater than 2% in the nanowire -termed the active region- with the adjoining pad regions -also termed barriers- under only $\sim 0.1\%$ strain. The fabrication process consists of a combination of electron-beam lithography on a Ge-on-insulator (GOI) wafer and dry and wet etching, as described in the previous chapter. HF vapor etch was used to create a fully suspended structure by removing the sacrificial oxide layer and this causes significant uniaxial strain concentration in the active region, while the strain in the barrier is reduced. By changing the length of the suspended barrier

regions with fixed active region geometry, various degrees of uniaxial strain along the [100] direction can be selectively induced in the active region. While the dimension of the active region was kept constant throughout this experiment, any arbitrary geometry of the active region can be used for creating pseudo-heterostructure nanowires since the strain level depends only on geometrical factors, such as the length and width ratios of the barrier and the active regions [70]. Because a large strain within the active region greatly reduces the electronic band gap and enables electron and hole confinement within deep potential wells (>50 meV for both electrons and holes at $\sim 2.3\%$ strain), this structure represents the first realization of double heterostructure behavior, that is capable of confining carriers at room temperature, within a single material. Figure 5.1(b) shows the electronic band profile along the active region of the nanowire pseudo double heterostructure. This band profile as well as the energy locations of the quasi-Fermi levels will play a central role in explaining the observed optical behavior of the pseudo-heterostructure nanowires. We will later quantify how photo-excited carriers in the barrier region diffuse into and are captured within the strain-induced potential well. This significantly increases the local carrier concentration within the active region, resulting in a spatially-confined, enhanced, and wavelength-shifted light emission from the strain-induced potential well.

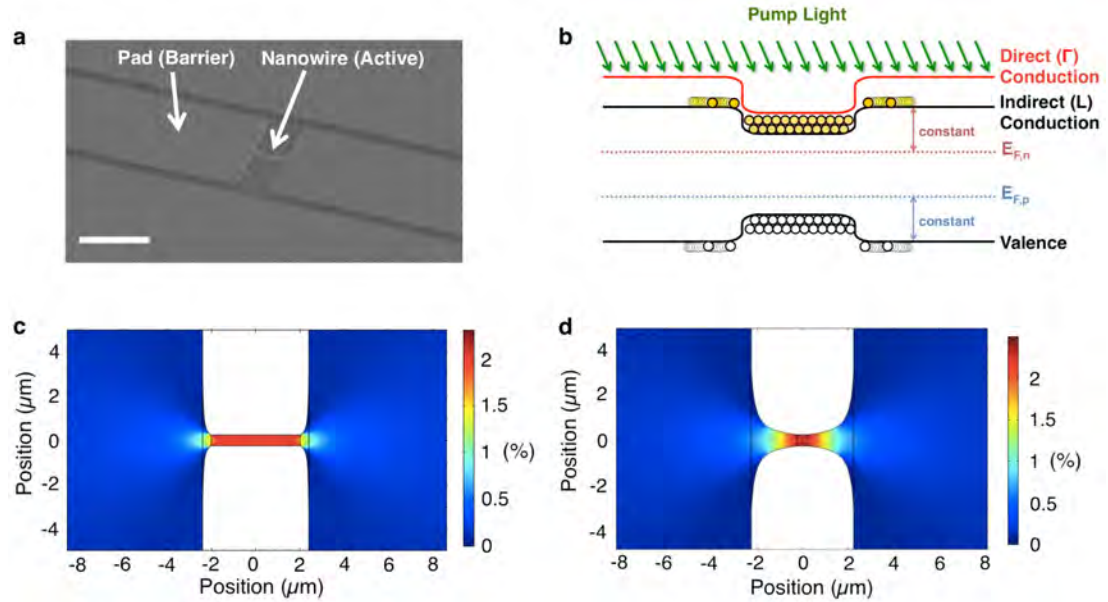


Figure 5.1 Strain-induced pseudo-heterostructure nanowires. (a) SEM image of a fabricated and fully suspended structure. Scale bar, 5 μm . (b) Schematic of the energy band diagram along the center of the structure showing a strain-induced potential well and captured carriers. Quasi-Fermi levels for electrons and holes are also indicated. (c) Finite-element COMSOL simulation for an s-DH. (d) Finite-element COMSOL simulation for an s-GDH.

Figures 5.1(c) and (d) show finite-element COMSOL simulations conducted to predict strain distributions in two pseudo-heterostructure nanowires with unique, engineered strain profiles: 1) a strain-induced double heterostructure (s-DH) and 2) a strain-induced graded double heterostructure (s-GDH). While the s-DH shows a relatively abrupt change in strain at the interface between the barrier and the active region, the strain in the s-GDH increases gradually towards the center of the active region. Since the strain in the active region is approximately inversely proportional to

the width at every point along the active region, we intentionally taper the width of the active region hyperbolically with position to create the s-GDH with an approximately linear strain gradient. Unlike the conventional way to make heterostructures, this method clearly presents extreme design flexibility to engineer heterostructure behavior with nanoscale-tunable electronic band profiles that may be hard to achieve via heteroepitaxy. Figure 5.2 shows finite-element COMSOL simulations of various pseudo-heterostructure nanowire designs.

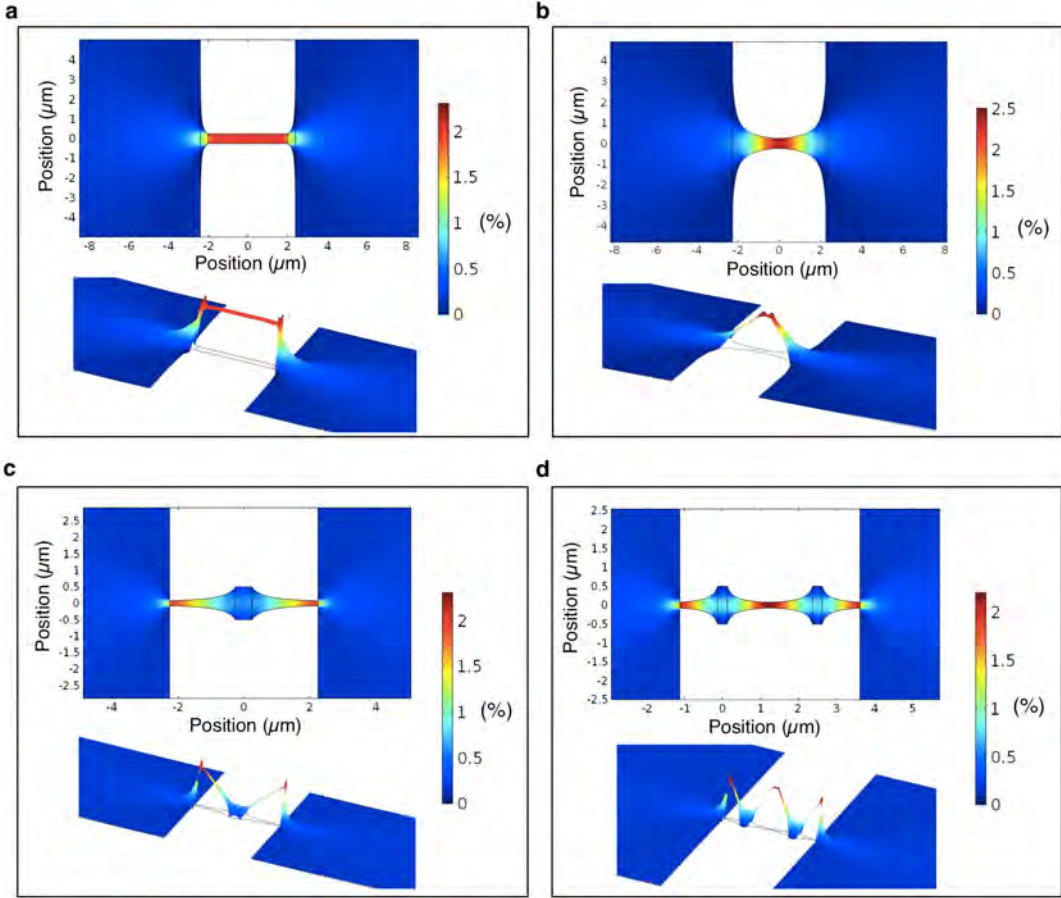


Figure 5.2 Finite-element COMSOL simulations of various pseudo-heterostructure designs. (a) Top-view and 3D projection of strain distribution in an s-DH. (b) Top-view and 3D projection of strain distribution in an s-GDH. (c,d) Top-views and 3D projections of strain distribution in alternative possible pseudo-heterostructures. Any locations with concentrated strain ($>2\%$) along the Ge nanowires have potential wells (>50 meV) deep enough to capture electrons and holes at room temperature. The units of the color bar represent uniaxial strain along the $[100]$ direction.

Figures 5.3(a) and (b) show SEM images of the s-DH and the s-GDH, respectively. The width of the active region in the s-DH is kept constant (~ 500 nm), while the s-GDH features a hyperbolically tapered width along the active region. Figures 5.3(c) and (d) show the 2D strain distributions of the two pseudo-heterostructure nanowires measured by Raman spectroscopy. An excitation laser with 514 nm wavelength was focused using a 100x objective lens. The spatial resolution for 2D strain mapping is expected to be 200 nm. The spectrum was fitted to a Lorentzian function and the relative shift from bulk Ge was calculated to obtain the strain in the samples [72], [79], [80]. The excitation laser power was kept to a minimum level to ensure no significant laser heating occurred during the measurements. In the s-DH, the strain abruptly increases in the active region and remains constant along it. On the other hand, the strain in the s-GDH gradually changes towards the center of the active region. As shown in the measured Raman shift spectrum in Figure 5.4, the strain in the barrier is slightly relaxed from 0.2% down to 0.1% while the strain in the active region

of the s-DH is significantly increased to 2.25%. The maximum strain at the center of the s-GDH is 2.30%. Figures 5.3(e) and (f) show the calculated spatial dependence of the band edges along the active region. To compute the band diagram along the main axis of the 2.25% strain s-DH and the 2.30% strain s-GDH, we first experimentally determined the strain profile along the axis by Raman spectroscopy. The strain profiles then allowed us to compute the band diagram from Ge's deformation potentials [17]. However, the interfaces between dissimilarly strained Ge regions results in some net charge which implies electric fields and band bending. We have thus employed a 1D finite-element Poisson solver to compute the band diagram along the pseudo-heterostructures, as shown in Figures 5.3(e) and (f) for the s-DH and s-GDH, respectively. From this analysis we find that the bands will bend strongly toward charge neutrality for both the s-DH and the s-GDH and so, after band bending, the conduction and valence offsets will be almost equal. Thus, the depth of the potential wells for both electrons and holes will be greater than 50 meV in the 2.25% s-DH and the 2.30% s-GDH. The s-DH presents a square-like potential well, whereas the s-GDH shows a graded potential well. With a clear type-I band offset in these structures and well-depths considerably exceeding kT , excited carriers (both electrons and holes) in the barriers will diffuse into and be captured within the potential well of the active region.

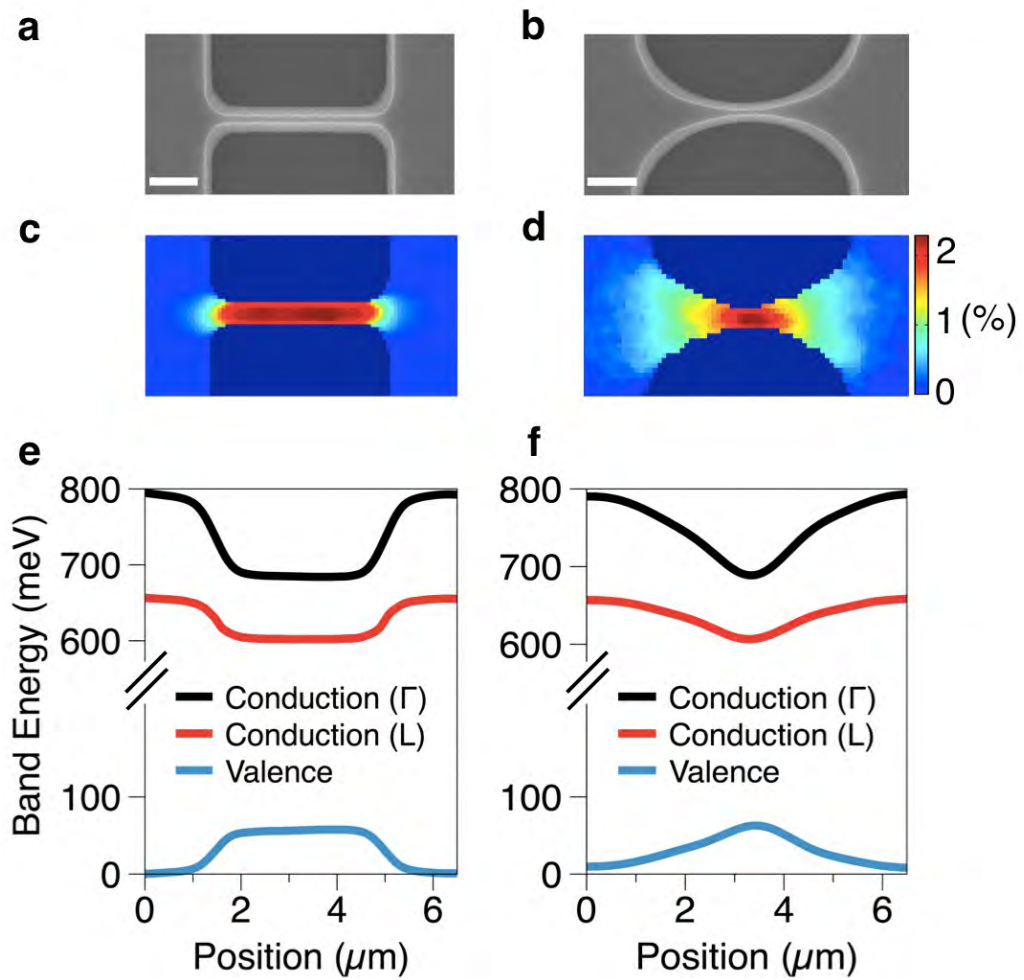


Figure 5.3 Pseudo-heterostructure nanowires with custom-designed band profiles at the nanoscale. (a) SEM image of a fabricated s-DH. Scale bar, 1 μm . (b) SEM image of a fabricated s-GDH. Scale bar, 1 μm . (c) 2D Raman strain mapping of an s-DH. (d) 2D Raman strain mapping of an s-GDH. The units of the color bar represent uniaxial strain along the [100] direction. (e) Calculated band diagram along the active region of the s-DH. (f) Calculated band diagram along the active region of the s-GDH.

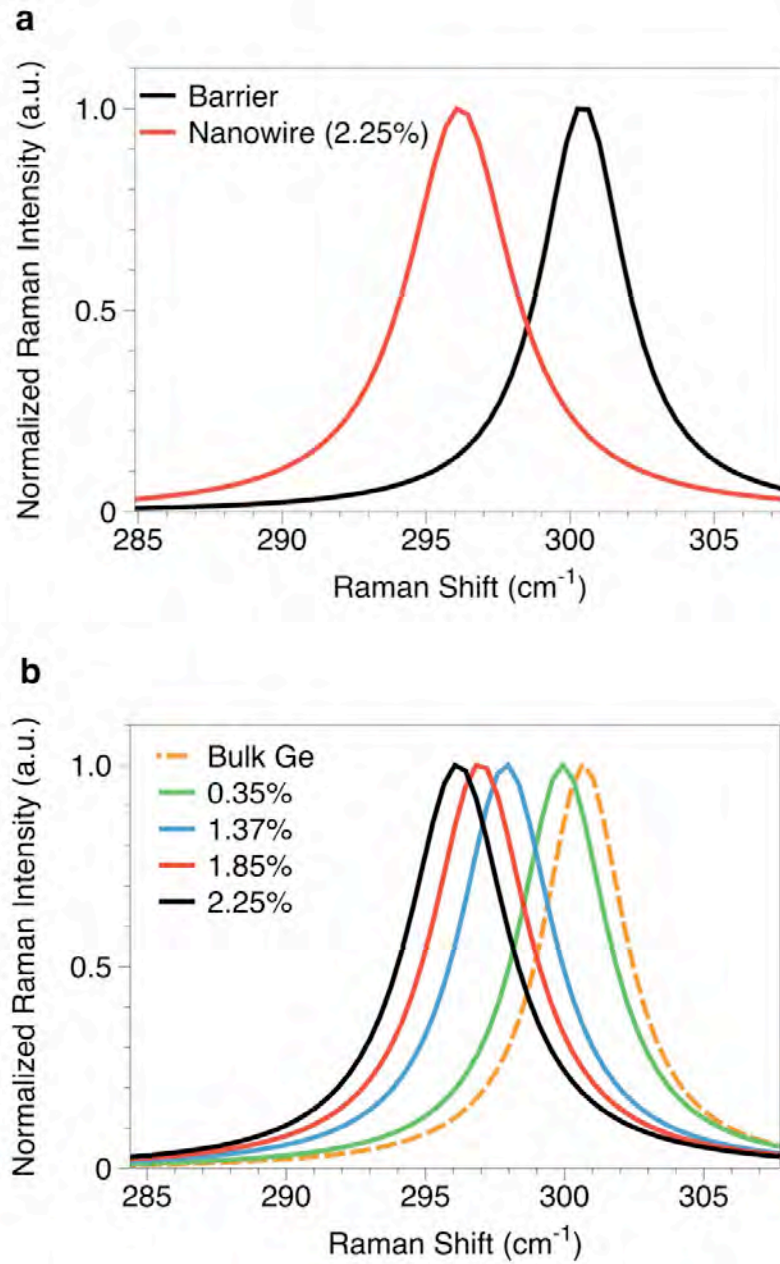


Figure 5.4 Raman spectra for active regions under various amounts of strain. (a) Measured Raman spectra for the barrier (black, 0.1% strain) and the active region (red, 2.25% strain) in an s-DH. (b) Measured Raman spectra for the active regions with various amounts of strains in s-DHs.

5.3 Light Emission from Strain-Induced Potential Wells

5.3.1 Spatially Confined Light Emission

In order to demonstrate the ability to confine carriers within the potential well of the active region, micro-photoluminescence (micro-PL) measurements were conducted. A continuous-wave (CW) laser with 532 nm wavelength was used to optically pump the material. The laser beam was slightly defocused using a 60x magnification lens to excite a relatively large area with a diameter of $\sim 15 \mu\text{m}$ in order to observe the carrier confinement effect. The integrated excitation power was < 2 mW to minimize heating effects. A strained InGaAs 1D-array detector (OMA-V series) from Princeton Instruments was used to perform measurements over an extended wavelength range. The quantum efficiency of the detector is nearly constant between $1.4 \mu\text{m}$ and $2.1 \mu\text{m}$. The detector cut-off was approximately $2.1 \mu\text{m}$, limiting detailed characterization of the 2.77%-strain nanowire. Figures 5.5(a) and (b) are optical images of the s-DH (with 2.25% strain along the active region) and the s-GDH (with 2.30% strain at the center of the active region). Figures 5.5(c) and (d) show the corresponding spatial photoluminescence (PL) maps for the s-DH and the s-GDH, respectively. Cross-sectional PL intensity variations along the active regions (along the broken white lines) are presented below.

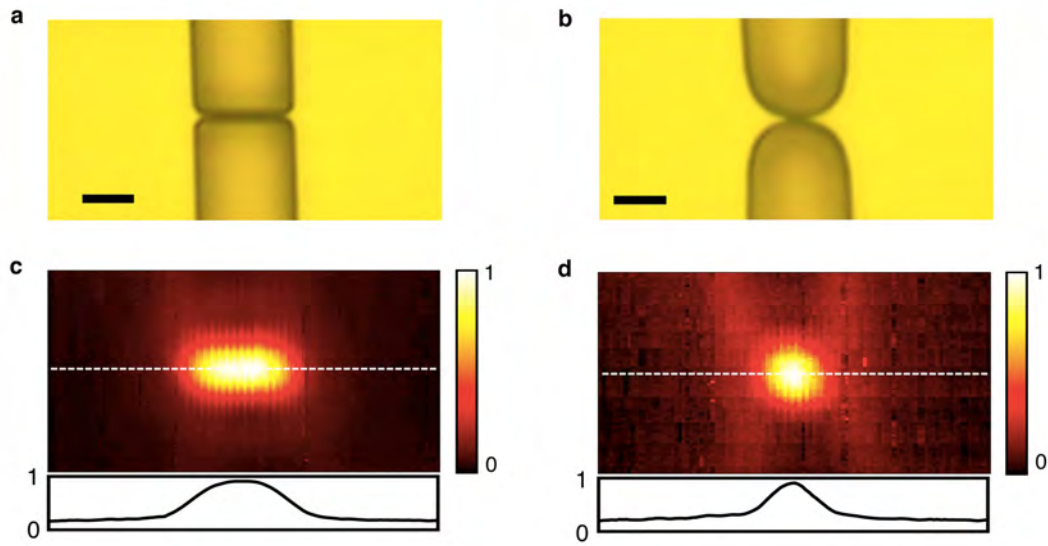


Figure 5.5 Spatially confined light emission from strain-induced potential wells. (a) Optical micrograph of an s-DH. Scale bar, 2 μm . (b) Optical micrograph of an s-GDH. Scale bar, 2 μm . (c) 2D photoluminescence (PL) map of an s-DH with 2.25% strain in the active region, showing bright emission along the active region. (d) 2D PL map of an s-GDH with 2.30% strain at the center of the active region, showing concentrated, bright emission at the center of the active region. The units of the color bar represent the normalized PL intensity. Insets in Figures 2(c) and (d) represent cross-sectional PL intensity variations along the active regions (along the white broken lines).

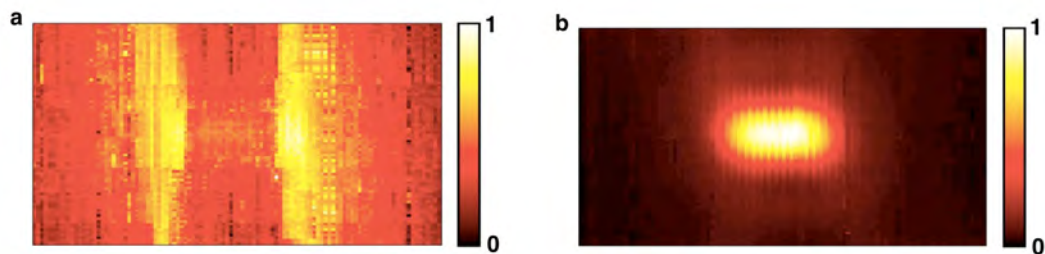


Figure 5.6 2D PL map comparison between shallow and deep potential wells. (a) 2D PL map of an s-DH with 0.35% strain in the active region, showing weaker emission along the active region due to the significant surface recombination and insignificant changes to the band diagram. (b) 2D PL map of an s-DH with 2.25% strain in the active region. The carrier confinement effect significantly increases the carrier concentration in the active region, thereby showing enhanced emission along the active region. The units for the color bar represent the normalized PL intensity.

In the 2.25%-strained s-DH, the carrier confinement effect significantly increases the carrier concentration in the active region, thereby showing much greater PL emission from the active region than from the barrier (Figure 5.5(c)). Because the depth of the potential well in the s-DH is approximately constant along the active region, the carriers captured within the potential well are uniformly distributed over the whole active region, resulting in enhanced emission from the entire width of the active region. It should be noted that, without the strong carrier confinement effect from the strain-induced potential well, the emission from the nanowire is weaker than the emission from its barrier because of the greater surface recombination in the nanowire (Figure 5.6). In the s-GDH, on the other hand, the gradients in the conduction and valence band edges force the electrons and holes into the center of the active region by setting up quasi-electric fields [99]. Therefore, the carrier concentration is greatly increased only at the center of the active region, leading to enhanced emission in the narrowest region (Figure 5.5(d)). We note that that these strain-induced pseudo-heterostructures are capable of concentrating carriers in any

desired locations along the nanowire. Tailoring the carrier concentrations within a compact area would be particularly beneficial for electrically injected semiconductor lasers. For instance, semiconductor lasers often use compositionally graded heterostructures to lower the lasing threshold by locally increasing the carrier density [100], [101].

5.3.2 Wavelength-Shifted, Enhanced Light Emission

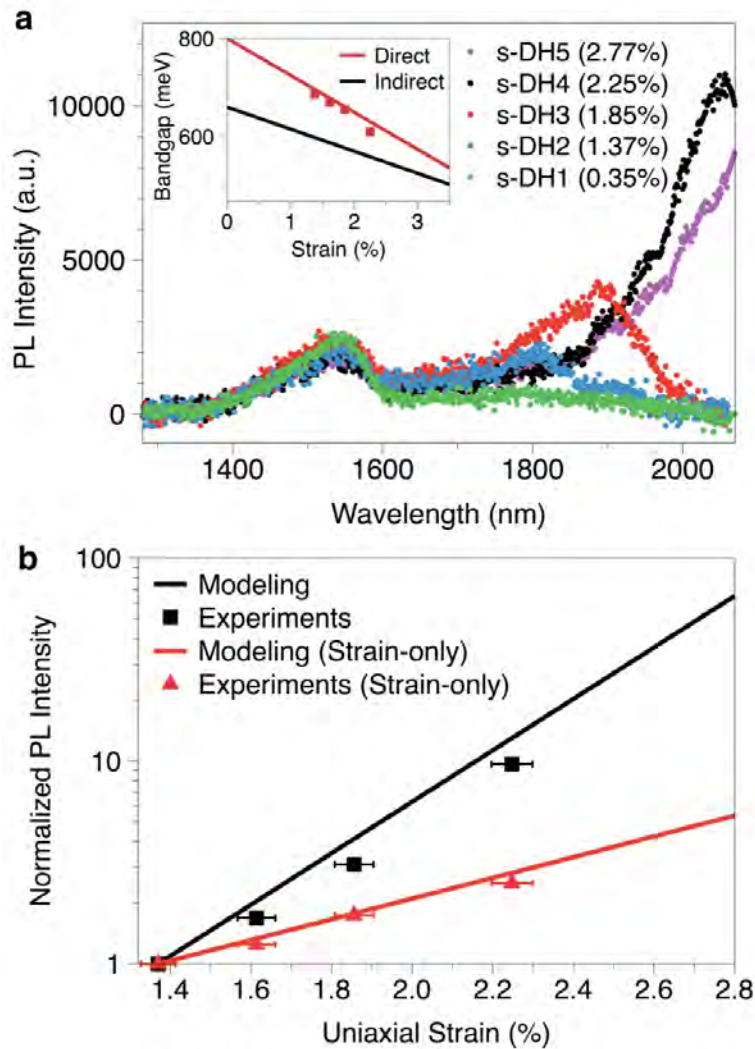


Figure 5.7 Enhanced and wavelength-shifted light emission from the strain-induced potential wells. (a) PL emission spectra from s-DHs with different strain levels in the active region. The same excitation level is used in all measurements. The inset shows the simulated band gap energies of the direct (red) and the indirect (black) band gaps. Experimental data points represent the measured peak emission energies from the active regions with different strains, and theoretical curves are from deformation potentials. (b) Theoretical PL enhancement with (black) and without (red) the carrier confinement effect. Experimental data points are shown as squares and triangles. Error bars in Figure 5.7(b) and in the inset to Figure 5.7(a) represent the root mean square (rms) errors between the Lorentzian fitting curves and the measured data.

To further verify the proper operation of these pseudo-heterostructure nanowires, we also analyzed how the spectral properties and intensity of the emission depend on the applied strain. Figure 5.7(a) shows PL spectra from s-DHs with various active region strain levels (the same optical excitation power was used in all cases). The emission from s-DH1 (strain in the active region: 0.35%) exhibits two peaks: one at 1.55 μm from the Ge direct gap transition and the other at 1.8 μm from the Ge indirect gap transition. Both of these peaks correspond mainly to emission from the lightly strained barrier region, as evidenced by the fact that this emission spectrum is identical to that from only the barrier. The emission from the 0.35%-strained active region is negligible because the active region has much less area than the barrier and because of significant surface recombination within the nanowire. With such a lightly strained

active region, the emission enhancement due to carrier concentration is not strong enough to make the active region emission comparable to the barrier emission. However, as the strain in the active region is increased, emission from it becomes significant while emission from the barrier does not change noticeably. The direct band gap emission from 1.37%, 1.85%, 2.25%, and 2.77% strained active regions corresponds to the long-wavelength peaks of spectra in Figure 5.7(a). The indirect band gap emission from the strained active regions was not observed because the emission wavelengths were redshifted beyond the detector cutoff of 2.10 μm due to band gap narrowing. Increasing the strain from 1.37% to 2.25% enhances the direct band gap emission by a factor of ~ 10 , while redshifting the peak wavelength to 2.05 μm . The emission spectrum from the 2.77%-strained active region is redshifted beyond the detector cut-off of 2.10 μm , showing only the tail of the spectrum. These experimentally observed redshifts of the emission peak-wavelengths are in good agreement with the predicted strain-induced band gap reductions shown in the inset of Figure 5.7(a).

Figure 5.7(b) shows the predicted PL emission enhancement from the active region due to the presence of the strain-induced potential well. For this modeling, the system is approximated as having flat quasi-Fermi levels for its steady state carrier distribution, as shown in Figure 5.1(b). This approximation of flat quasi-Fermi levels is justified if the carrier diffusion length in Ge is longer than the 4.5 μm length of the active region. Pessimistically assuming a minority carrier lifetime in Ge of $\tau \approx 10$ ns, an order of magnitude less than commonly used [21], and a carrier diffusion coefficient

of $D \approx 50 \text{ cm}^2/\text{s}$ [22], we compute a diffusion length of $7.1 \text{ }\mu\text{m}$. A further approximation can be made that the carrier densities in the barrier will be roughly constant even as the active region strain increases. This is justified by the fact that the barrier region is $>100x$ larger than the active region. Given these assumptions of flat and constant quasi-Fermi levels, we can take the carrier concentrations for holes, electrons, and electrons in the direct (Γ) conduction valley in the active region to be:

$$p = N_v \cdot \exp[(E_v - E_{fp})/kT]$$

$$n = N_c \cdot \exp[(E_{fn} - E_{c,L})/kT]$$

$$n_\Gamma = N_{c,\Gamma} \cdot \exp[(E_{fn} - E_{c,\Gamma})/kT]$$

p , n , and n_Γ are carrier concentrations for holes, electrons, and electrons in the direct (Γ) band gap, respectively. N_v , N_c , and $N_{c,\Gamma}$ are the effective density of states for holes, electrons, and the direct (Γ) conduction valley, respectively. E_v , $E_{c,L}$, and $E_{c,\Gamma}$ are the energies for the valence band edge, the indirect (L) conduction band edge, and the direct (Γ) conduction band edge. E_{fp} and E_{fn} are quasi-Fermi levels for holes and electrons, k is the Boltzmann constant, and T is the absolute temperature. Given a radiative recombination coefficient R , and ignoring emission from the indirect transition, the emission rate will be given by:

$$\text{emission rate} = R \cdot n_\Gamma \cdot p$$

$$\text{emission rate} = R \cdot N_{c,\Gamma} \cdot \exp[(E_{fn} - E_{c,\Gamma})/kT] \cdot N_v \cdot \exp[(E_v - E_{fp})/kT]$$

$$\text{emission rate} = R \cdot N_{c,\Gamma} \cdot N_v \cdot \exp[(E_{fn} - E_{fp})/kT] \cdot \exp[(E_v - E_{c,\Gamma})/kT]$$

$$\text{emission rate} = R \cdot N_{c,\Gamma} \cdot N_v \cdot \exp[(E_{fn} - E_{fp})/kT] \cdot \exp[-E_{g,\Gamma}/kT]$$

$$\text{emission rate} \sim \exp[-E_{g,\Gamma}/kT] \quad (1)$$

It is therefore predicted that the PL will increase exponentially as the direct band gap ($E_{g,\Gamma}$) decreases in accordance with equation (1). Squares represent experimentally measured active region emission peak intensities normalized to the emission from the active region of the 1.37%-strained s-DH. Our model (solid line) predicts an emission enhancement of 18x for every 1% increase in uniaxial strain with carrier confinement in the s-DHs. This is in good agreement with the experimental fit to the measured data points (squares) presenting an enhancement of 14x for every 1% increase in strain. The slightly smaller measured enhancement compared to the theoretical prediction may be caused by greater surface recombination in the active region.

Since strain alone also enhances light emission slightly by reducing the energy difference between the direct and the indirect band gap as shown in the inset of Figure 5.7(a), the emission enhancement only by strain is also predicted. Without the heterostructure effect, the emission rate is give by:

$$\text{emission rate} = R \cdot n_{\Gamma} \cdot p$$

$$\text{emission rate} = R \cdot n \cdot p \cdot (n_{\Gamma}/n)$$

$$\text{emission rate} = R \cdot n \cdot p \cdot$$

$$(N_{c,\Gamma} \cdot \exp[(E_{fn} - E_{c,\Gamma})/kT]) / (N_c \cdot \exp[(E_{fn} - E_{c,L})/kT])$$

$$\text{emission rate} = R \cdot n \cdot p \cdot (N_{c,\Gamma}/N_c) \cdot \exp[(E_{c,L} - E_{c,\Gamma})/kT]$$

$$\text{emission rate} \sim \exp[(E_{c,L} - E_{c,\Gamma})/kT] \quad (2)$$

This again shows an exponential dependence, but a much weaker one than for the previous case. Specifically, since every 1% of tensile strain reduces ($E_{g,\Gamma} - E_{c,L}$) by ~30 meV according to deformation potential theory [17], this corresponds to a ~3x

enhancement of the PL for every 1% of strain at 300 K, shown as the red solid curve in Figure 5.7(b). Experimental data points in red triangles representing the enhancement only due to strain were measured by tightly focusing the optical pumping exclusively onto the active region in order to prevent carriers diffusing in from the barrier. The experimental fit to the measured data points (triangles) is also in good agreement with the experiments. Since the total enhancement is 14x per 1% strain, an additional $\sim 5x$ enhancement for every 1% strain from the pseudo-heterostructure nanowire can be attributed to the carrier confinement effect within the potential well of the active region. Since the emission from the strain-induced potential well is enhanced exponentially by strain, we infer that $\sim 2.3\%$ strain increases the PL emission from the pseudo-heterostructure nanowire by $>200x$ compared to the unstrained case.

5.3.3 PL Emission Dependence on Excitation Locations

To offer a further proof that carrier confinement is taking place in these strain-induced heterostructures, we measure the PL intensity distribution of the s-DH with the 2.25%-strained active region while moving the position of the optical pump. Figure 5.8(a) is an optical micrograph of a typical s-DH with green circles indicating the different positions of the optical pump beam, labeled as (1), (2), and (3). When the excitation covers the center region (Figure 5.8(b)), emission from the active region is greatly enhanced, dominating emission from the barrier. With the excitation beam offset from the center (Figure 5.8(c)), broad emission from the barrier is clearly

observed because excited carriers are piled up in the vicinity of the excitation area and recombine radiatively. However, as some of the excited carriers diffuse, those reaching the nanowire are captured within the potential well, resulting in enhanced emission at the active region. As shown in Figure 5.8(d), a sharp increase in emission appears at the active region even when there is no significant emission at the immediately adjacent barrier region, proving that most carriers around the potential well diffuse into and are captured within the potential well. Figure 5.8(e) shows that the emission from the active region is at much longer wavelength ($\sim 2.05 \mu\text{m}$) than the emission from the barrier ($\sim 1.55 \mu\text{m}$). We expect that employing this heterostructure in lateral electrically-driven light-emitting diodes can greatly enhance the light emission efficiency because carriers can be effectively captured in the intrinsic potential well, with minimal recombination at P- and N-type doped regions.

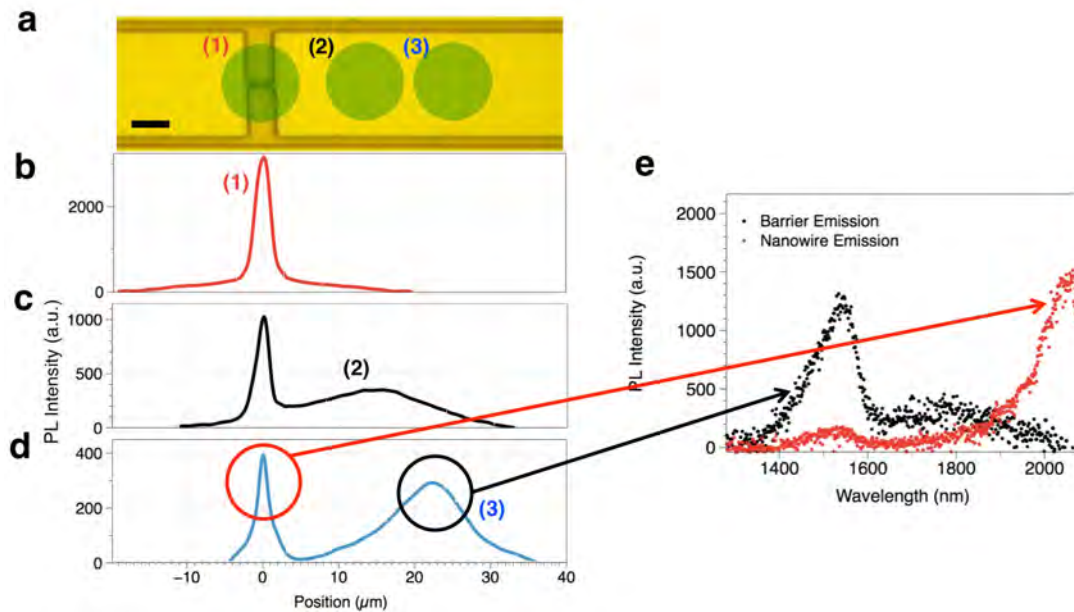


Figure 5.8 PL emission dependence on excitation locations. (a) Optical image of an s-DH with a 2.25%-strain active region. Three different excitation locations are shown as green circles with labels (1), (2), and (3). The size of the circles represents an approximate excitation area. Scale bar, 5 μm . (b) PL emission as a function of position along the horizontal axis with excitation located at circle (1). (c) PL emission with excitation located at circle (2). (d) PL emission with excitation located at circle (3). (e) PL spectra from the barrier region (black) and the active region (red). The active region emission is at much longer wavelength ($\sim 2.05 \mu\text{m}$) than the barrier emission ($\sim 1.55 \mu\text{m}$).

5.4 Conclusion

In this chapter, we presented a novel concept of single material pseudo-heterostructure nanowires with custom-designed electronic band profiles by tuning strain profiles at the nanoscale. Strain-induced pseudo-heterostructures with potential well depths exceeding kT enabled strong carrier confinement within highly strained nanowires at room temperature. We have experimentally validated this concept by demonstrating spatially-confined, enhanced, and wavelength shifted light emission from the nanowires. Although only uniaxial strain along the [100] direction was investigated in this experiment, it should be noted that other directions and types of tensile strain, such as uniaxial strain along the [110] and [111] directions, biaxial strain and hydrostatic strain, can also induce deep and localized potential wells for creating pseudo-heterostructures with different deformation potentials [17].

One immediate application for this work is in double-heterostructure nanolasers, both because of recent interest in Ge lasers [54], [55] and because this approach is expected to be very general and should be transferable to III-V materials which have been used extensively as laser gain media [91], [102]. The ability to achieve multiple heterostructures with different band gaps on a single die should enable the creation of integrated multi-wavelength light sources. This could be as simple as multi-color or white LEDs [103], or as involved as dense wavelength division multiplexing for optical interconnects by accessing a wide range of band gaps [8], [104]. Heterostructure electronics are yet another possibility, for instance serving to achieve high injection velocities from a wide-bandgap region into a narrow-bandgap region in nanowire FETs [105]. At the most general level, the presented approach represents a fundamentally new paradigm for creating nanoscale devices with full heterostructure behavior which previously required multiple semiconductor materials grown on top of each other. It not only reduces the fabrication complexities associated with integrating high-quality layers of different semiconductor materials, but also introduces unprecedented design flexibility for creating nanoscale heterostructures.

Chapter 6

Conclusions & Future Works

In this dissertation, we introduced strained germanium (Ge) technology for an efficient light source that may enable the completion of on-chip optical interconnects link. Although theoretical calculations have revealed the possibility of greatly improved light emission from highly strained Ge, little research has been conducted to employ such a large strain to Ge using a CMOS-compatible approach.

In the first part, therefore, our efforts were spent developing a technology platform to induce a large tensile strain to Ge by creating a thin Ge membrane integrated on a Si substrate. By depositing a stressor layer on the thin membrane, the residual stress in the stressor layer was successfully transferred to Ge, resulting in a large biaxial strain greater than 1%. Photoluminescence (PL) measurements revealed the enhanced light emission from strained Ge membranes and we discussed the

implication of the improved optical properties towards creating an efficient laser for on-chip optical interconnects. In addition, we demonstrated the first optoelectronic devices integrated on the highly strained Ge membranes to show the practicality of our technique.

In the second part, we presented a radically new, fully CMOS-compatible approach to apply a large uniaxial tensile strain to Ge wires using geometrical amplification of a small pre-existing biaxial strain. We demonstrated the fabrication of a Ge-on-Insulator wafer with a high-quality Ge film which enabled the creation of a highly localized strain in a Ge wire by simply removing the thin sacrificial oxide layer. The full carrier dynamics associated with the valence band splitting was studied using several types of PL measurements which allowed us to clearly observe the light emissions from different band-to-band optical transitions. We also presented theoretical modeling of how these improved carrier dynamics in uniaxially strained Ge can help pave the way towards an efficient Ge light source for optical interconnects.

In the last part, we presented a novel concept of creating strain-induced potential wells with tunable electronic band profiles at the nanoscale. The ability to create a custom-designed strain distribution within a Ge nanowire enabled tailoring the photo-excited carrier distribution within a single material. This new concept of mimicking a heterostructure behavior by strain engineering was experimentally validated by demonstrating spatially-confined, enhanced, and wavelength shifted light emission from the nanowires.

Throughout this dissertation, we demonstrated two essential components of a laser: an efficient gain material and heterostructure. In particular, strained Ge nanowires introduced in the later chapters allowed us to achieve both components in the same physical space by inducing a high, localized strain within a compact area. By incorporating a proper optical cavity into this Ge structure that can achieve multiple functions at the same time, an efficient Ge laser may be realized in the near future to complete an on-chip optical interconnects system.

Bibliography

- [1] R. H. Dennard, F. H. Gaensslen, H. Yu, V. L. Rideout, E. Bassous, and A. R. LeBlank, "Design of ion-implanted MOSFET's with very small physical dimensions," *Solid-State Circuits*, vol. SC-9, pp. 256–258, 1974.
- [2] K. C. Saraswat and F. Mohammadi, "Effect of scaling of interconnections on the time delay of VLSI circuits," *IEEE J. Solid-State Circuits*, vol. 17, no. 2, pp. 275–280, Apr. 1982.
- [3] N. Magen, A. Kolodny, U. Weiser, and N. Shamir, "Interconnect-power dissipation in a microprocessor," *Proc. 2004 Int. Work. Syst. Lev. Interconnect Predict. (ACM, 2004) Sess. Interconnect Anal. SoCs Microprocess.*, pp. 7–13, 2004.
- [4] M. Paniccia and J. Bower, "First electrically pumped hybrid silicon laser," pp. 1–27, 2006.
- [5] B. J. Offrein, "Optical interconnects for computing applications," *SEREC*, 2009.
- [6] D. A. B. Miller, "Rationale and challenges for optical interconnects to electronic chips," *Proc. IEEE*, vol. 88, no. 6, pp. 728–749, Jun. 2000.
- [7] K.-H. Koo, P. Kapur, and K. C. Saraswat, "Compact performance models and comparisons for gigascale on-chip global interconnect technologies," *IEEE Trans. Electron Devices*, vol. 56, no. 9, pp. 1787–1798, Sep. 2009.
- [8] D. A. B. Miller, "Device requirements for optical interconnects to silicon chips," *Proc. IEEE*, vol. 97, no. 7, pp. 1166–1185, 2009.

- [9] G. Chen, H. Chen, M. Haurylau, N. Nelson, P. M. Fauchet, and E. G. Friedman, "Predictions of CMOS compatible on-chip optical interconnect," *Int. Work. Syst. Lev. Interconnect Predict.*, p. 13, 2005.
- [10] Y.-H. Kuo, Y. K. Lee, Y. Ge, S. Ren, J. E. Roth, T. I. Kamins, D. A. B. Miller, and J. S. Harris, "Strong quantum-confined Stark effect in germanium quantum-well structures on silicon," *Nature*, vol. 437, no. 7063, pp. 1334–6, Oct. 2005.
- [11] S. Klinger, M. Berroth, M. Kaschel, M. Oehme, and E. Kasper, "Ge-on-Si p-i-n photodiodes with a 3-dB bandwidth of 49 GHz," *IEEE Photonics Technol. Lett.*, vol. 21, no. 13, pp. 920–922, 2009.
- [12] L. Vivien, A. Polzer, D. Marris-Morini, J. Osmond, J. M. Hartmann, P. Crozat, E. Cassan, C. Kopp, H. Zimmermann, and J. M. Fédéli, "Zero-bias 40Gbit/s germanium waveguide photodetector on silicon," *Opt. Express*, vol. 20, no. 2, pp. 1096–101, Jan. 2012.
- [13] M. Jutzi, M. Berroth, G. Wöhl, M. Oehme, and E. Kasper, "Ge-on-Si vertical incidence photodiodes with 39-GHz bandwidth," *IEEE Photonics Technol. Lett.*, vol. 17, no. 7, pp. 1510–1512, 2005.
- [14] P. Chaisakul, D. Marris-Morini, M.-S. Rouifed, G. Isella, D. Chrastina, J. Frigerio, X. Le Roux, S. Edmond, J.-R. Coudevylle, and L. Vivien, "23 GHz Ge/SiGe multiple quantum well electro-absorption modulator," *Opt. Express*, vol. 20, no. 3, pp. 3219–24, Jan. 2012.
- [15] P. H. Lim, S. Park, Y. Ishikawa, and K. Wada, "Enhanced direct bandgap emission in germanium by micromechanical strain engineering," *Opt. Express*, vol. 17, no. 18, pp. 16358–65, Aug. 2009.
- [16] M. V. Fischetti and S. E. Laux, "Band structure, deformation potentials, and carrier mobility in strained Si, Ge, and SiGe alloys," *J. Appl. Phys.*, vol. 80, no. 4, p. 2234, 1996.
- [17] C. G. Van der Walle, "Band lineups and deformation potentials in the model-solid theory," *Physical review B*, vol. 39, no. 3, pp. 1871–1883, 1989.
- [18] J. Michel, J. Liu, and L. C. Kimerling, "High-performance Ge-on-Si photodetectors," *Nat. Photonics*, vol. 4, no. 8, pp. 527–534, Jul. 2010.
- [19] Y. Kang, H.-D. Liu, M. Morse, M. J. Paniccia, M. Zadka, S. Litski, G. Sarid, A. Pauchard, Y.-H. Kuo, H.-W. Chen, W. S. Zaoui, J. E. Bowers, A. Beling, D. C. McIntosh, X. Zheng, and J. C. Campbell, "Monolithic germanium/silicon

- avalanche photodiodes with 340 GHz gain–bandwidth product,” *Nat. Photonics*, vol. 3, no. December 2008, pp. 59–63, 2008.
- [20] S. Assefa, F. Xia, and Y. A. Vlasov, “Reinventing germanium avalanche photodetector for nanophotonic on-chip optical interconnects,” *Nature*, vol. 464, no. 7285, pp. 80–4, Mar. 2010.
- [21] H.-Y. Yu, S. Ren, W. S. Jung, A. K. Okyay, D. A. B. Miller, and K. C. Saraswat, “High-efficiency p-i-n photodetectors on selective-area-grown Ge for monolithic integration,” *IEEE Electron Device Lett.*, vol. 30, no. 11, pp. 1161–1163, Nov. 2009.
- [22] A. K. Okyay, A. M. Nayfeh, K. C. Saraswat, T. Yonehara, A. Marshall, and P. C. McIntyre, “High-efficiency metal-semiconductor-metal photodetectors on heteroepitaxially grown Ge on Si,” *Opt. Lett.*, vol. 31, no. 17, pp. 2565–7, Sep. 2006.
- [23] G. E. Stillman, V. M. Robbins, and N. Tabatabaie, “III-V compound semiconductor devices : optical detectors,” *IEEE Trans. Electron Devices*, vol. 31, no. 11, pp. 1643–1655, 1984.
- [24] T.-H. Cheng, K.-L. Peng, C.-Y. Ko, C.-Y. Chen, H.-S. Lan, Y.-R. Wu, C. W. Liu, and H.-H. Tseng, “Strain-enhanced photoluminescence from Ge direct transition,” *Appl. Phys. Lett.*, vol. 96, no. 21, p. 211108, 2010.
- [25] J. Liu, X. Sun, D. Pan, X. Wang, L. C. Kimerling, T. L. Koch, and J. Michel, “Tensile-strained, n-type Ge as a gain medium for monolithic laser integration on Si,” *Opt. Express*, vol. 15, no. 18, pp. 11272–7, Sep. 2007.
- [26] X. Sun, J. Liu, L. C. Kimerling, and J. Michel, “Direct gap photoluminescence of n-type tensile-strained Ge-on-Si,” *Appl. Phys. Lett.*, vol. 95, no. 1, p. 011911, 2009.
- [27] S. Cheng, J. Lu, G. Shambat, H.-Y. Yu, K. C. Saraswat, J. Vučković, and Y. Nishi, “Room temperature 1.6 μm electroluminescence from Ge light emitting diode on Si substrate,” *Opt. Express*, vol. 17, no. 12, pp. 10019–24, Jun. 2009.
- [28] M. El Kurdi, T. Kociniewski, T.-P. Ngo, J. Boulmer, D. Débarre, P. Boucaud, J. F. Damlencourt, O. Kermarrec, and D. Bensahel, “Enhanced photoluminescence of heavily n-doped germanium,” *Appl. Phys. Lett.*, vol. 94, no. 19, p. 191107, 2009.
- [29] S. Gupta, R. Chen, Y.-C. Huang, Y. Kim, E. Sanchez, J. S. Harris, and K. C. Saraswat, “Highly selective dry etching of germanium over germanium–tin

- (Ge_{1-x}Sn_x): A novel route for Ge_{1-x}Sn_x nanostructure fabrication,” *Nano Lett.*, Jul. 2013.
- [30] S. Gupta, B. Magyari-Köpe, Y. Nishi, and K. C. Saraswat, “Achieving direct band gap in germanium through integration of Sn alloying and external strain,” *J. Appl. Phys.*, vol. 113, no. 7, p. 073707, 2013.
- [31] R. Chen, H. Lin, Y. Huo, C. Hitzman, T. I. Kamins, and J. S. Harris, “Increased photoluminescence of strain-reduced, high-Sn composition Ge_{1-x}Sn_x alloys grown by molecular beam epitaxy,” *Appl. Phys. Lett.*, vol. 99, no. 18, p. 181125, 2011.
- [32] M. El Kurdi, G. Fishman, S. Sauvage, and P. Boucaud, “Band structure and optical gain of tensile-strained germanium based on a 30 band k·p formalism,” *J. Appl. Phys.*, vol. 107, no. 1, p. 013710, 2010.
- [33] P. Boucaud, M. El Kurdi, A. Ghrib, M. Prost, M. de Kersauson, S. Sauvage, F. Aniel, X. Chécoury, G. Beaudoin, L. Largeau, I. Sagnes, G. Ndong, M. Chaigneau, and R. Ossikovski, “Recent advances in germanium emission,” *Photonics Res.*, vol. 1, no. 3, pp. 102–109, 2013.
- [34] G.-E. Chang and H. H. Cheng, “Optical gain of germanium infrared lasers on different crystal orientations,” *J. Phys. D: Appl. Phys.*, vol. 46, no. 6, p. 065103, Feb. 2013.
- [35] Y.-Y. Fang, J. Tolle, R. Roucka, A. V. G. Chizmeshya, J. Kouvetakis, V. R. D’Costa, and J. Menéndez, “Perfectly tetragonal, tensile-strained Ge on Ge_{1-y}Sn_y buffered Si(100),” *Appl. Phys. Lett.*, vol. 90, no. 6, p. 061915, 2007.
- [36] H. Lin, R. Chen, W. Lu, Y. Huo, T. I. Kamins, and J. S. Harris, “Structural and optical characterization of Si_xGe_{1-x-y}Sn_y alloys grown by molecular beam epitaxy,” *Appl. Phys. Lett.*, vol. 100, no. 14, p. 141908, 2012.
- [37] Y. Bai, K. E. Lee, C. Cheng, M. L. Lee, and E. A. Fitzgerald, “Growth of highly tensile-strained Ge on relaxed In_xGa_{1-x}As by metal-organic chemical vapor deposition,” *J. Appl. Phys.*, vol. 104, no. 8, p. 084518, 2008.
- [38] S.-L. Cheng, G. Shambat, J. Lu, H.-Y. Yu, K. Saraswat, T. I. Kamins, J. Vuckovic, and Y. Nishi, “Cavity-enhanced direct band electroluminescence near 1550 nm from germanium microdisk resonator diode on silicon,” *Appl. Phys. Lett.*, vol. 98, no. 21, p. 211101, 2011.

- [39] G. Shambat, S.-L. Cheng, J. Lu, Y. Nishi, and J. Vuckovic, "Direct band Ge photoluminescence near 1.6 μm coupled to Ge-on-Si microdisk resonators," *Appl. Phys. Lett.*, vol. 97, no. 24, p. 241102, 2010.
- [40] D. Nam, D. Sukhdeo, A. Roy, K. Balram, S.-L. Cheng, K. C.-Y. Huang, Z. Yuan, M. Brongersma, Y. Nishi, D. Miller, and K. Saraswat, "Strained germanium thin film membrane on silicon substrate for optoelectronics," *Opt. Express*, vol. 19, no. 27, pp. 25866–72, 2011.
- [41] B. Dutt, D. S. Sukhdeo, D. Nam, B. M. Vulovic, and K. C. Saraswat, "Roadmap to an efficient germanium-on-silicon laser: strain vs. n-type doping," *IEEE Photonics J.*, vol. 4, no. 5, pp. 2002–2009, Oct. 2012.
- [42] J. R. Sánchez-Pérez, C. Boztug, F. Chen, F. F. Sudradjat, D. M. Paskiewicz, R. B. Jacobson, M. G. Lagally, and R. Paiella, "Direct-bandgap light-emitting germanium in tensilely strained nanomembranes," *Proc. Natl. Acad. Sci. U. S. A.*, vol. 108, no. 47, pp. 18893–8, 2011.
- [43] D. Nam, D. Sukhdeo, S.-L. Cheng, A. Roy, K. Chih-Yao Huang, M. Brongersma, Y. Nishi, and K. Saraswat, "Electroluminescence from strained germanium membranes and implications for an efficient Si-compatible laser," *Appl. Phys. Lett.*, vol. 100, no. 13, p. 131112, 2012.
- [44] M. El Kurdi, H. Bertin, E. Martincic, M. De Kersauson, G. Fishman, S. Sauvage, A. Bosseboeuf, and P. Boucaud, "Control of direct band gap emission of bulk germanium by mechanical tensile strain," *Appl. Phys. Lett.*, vol. 96, no. 4, p. 041909, 2010.
- [45] A. Ghrib, M. de Kersauson, M. El Kurdi, R. Jakomin, G. Beaudoin, S. Sauvage, G. Fishman, G. Ndong, M. Chaigneau, R. Ossikovski, I. Sagnes, and P. Boucaud, "Control of tensile strain in germanium waveguides through silicon nitride layers," *Appl. Phys. Lett.*, vol. 100, no. 20, p. 201104, 2012.
- [46] M. de Kersauson, M. El Kurdi, S. David, X. Checoury, G. Fishman, S. Sauvage, R. Jakomin, G. Beaudoin, I. Sagnes, and P. Boucaud, "Optical gain in single tensile-strained germanium photonic wire," *Opt. Express*, vol. 19, no. 19, pp. 17925–34, Sep. 2011.
- [47] G. Capellini, G. Kozlowski, Y. Yamamoto, M. Lisker, T. Schroeder, A. Ghrib, M. de Kersauson, M. El Kurdi, P. Boucaud, and B. Tillack, "Tensile strained Ge layers obtained via a Si-CMOS compatible approach," *2012 Int. Silicon-Germanium Technol. Device Meet.*, pp. 1–2, Jun. 2012.

- [48] T.-H. Cheng, C.-Y. Ko, C.-Y. Chen, K.-L. Peng, G.-L. Luo, C. W. Liu, and H.-H. Tseng, "Competitiveness between direct and indirect radiative transitions of Ge," *Appl. Phys. Lett.*, vol. 96, no. 9, p. 091105, 2010.
- [49] G. Capellini, G. Kozlowski, Y. Yamamoto, M. Lisker, C. Wenger, G. Niu, P. Zaumseil, B. Tillack, A. Ghrib, M. de Kersauson, M. El Kurdi, P. Boucaud, and T. Schroeder, "Strain analysis in SiN/Ge microstructures obtained via Si-complementary metal oxide semiconductor compatible approach," *J. Appl. Phys.*, vol. 113, no. 1, p. 013513, 2013.
- [50] Y. Ishikawa, K. Wada, D. D. Cannon, J. Liu, H.-C. Luan, and L. C. Kimerling, "Strain-induced band gap shrinkage in Ge grown on Si substrate," *Appl. Phys. Lett.*, vol. 82, no. 13, p. 2044, 2003.
- [51] A. Nayfeh, C. O. Chui, T. Yonehara, and K. C. Saraswat, "Fabrication of high-quality p-MOSFET in Ge grown heteroepitaxially on Si," *IEEE Electron Device Lett.*, vol. 26, no. 5, pp. 311–313, 2005.
- [52] A. Nayfeh, C. O. Chui, K. C. Saraswat, and T. Yonehara, "Effects of hydrogen annealing on heteroepitaxial-Ge layers on Si: Surface roughness and electrical quality," *Appl. Phys. Lett.*, vol. 85, no. 14, p. 2815, 2004.
- [53] A. K. Okyay, A. M. Nayfeh, K. C. Saraswat, A. Marshall, and P. C. McIntyre, "Ge on Si by novel heteroepitaxy for high efficiency near infrared photodetection," in *Conference on Lasers and Electro-Optics (CLEO)*, vol. 2, pp. 4–5, 2006.
- [54] R. E. Camacho-Aguilera, Y. Cai, N. Patel, J. T. Bessette, M. Romagnoli, L. C. Kimerling, and J. Michel, "An electrically pumped germanium laser," *Opt. Express*, vol. 20, no. 10, pp. 11316–20, 2012.
- [55] J. Liu, X. Sun, R. Camacho-Aguilera, L. C. Kimerling, and J. Michel, "Ge-on-Si laser operating at room temperature," *Opt. Lett.*, vol. 35, no. 5, pp. 679–81, Mar. 2010.
- [56] M. H. Liao, P.-S. Kuo, S.-R. Jan, S. T. Chang, and C. W. Liu, "Strained Pt Schottky diodes on n-type Si and Ge," *Appl. Phys. Lett.*, vol. 88, no. 14, p. 143509, 2006.
- [57] C. Boztug, J. R. Sánchez-Pérez, F. F. Sudradjat, R. B. Jacobson, D. M. Paskiewicz, M. G. Lagally, and R. Paiella, "Tensilely strained germanium nanomembranes as infrared optical gain media," *Small*, vol. 9, no. 4, pp. 622–30, Feb. 2013.

- [58] Y. Huo, H. Lin, R. Chen, M. Makarova, Y. Rong, M. Li, T. I. Kamins, J. Vuckovic, and J. S. Harris, "Strong enhancement of direct transition photoluminescence with highly tensile-strained Ge grown by molecular beam epitaxy," *Appl. Phys. Lett.*, vol. 98, no. 1, p. 011111, 2011.
- [59] L. Nataraj, F. Xu, and S. G. Cloutier, "Direct-bandgap luminescence at room-temperature from highly-strained Germanium nanocrystals," *Opt. Express*, vol. 18, no. 7, pp. 7085–91, Mar. 2010.
- [60] T. Boykin, N. Kharche, and G. Klimeck, "Brillouin-zone unfolding of perfect supercells having nonequivalent primitive cells illustrated with a Si/Ge tight-binding parameterization," *Phys. Rev. B*, vol. 76, pp. 1–7, 2007.
- [61] T. Boykin, G. Klimeck, R. Bowen, and F. Oyafuso, "Diagonal parameter shifts due to nearest-neighbor displacements in empirical tight-binding theory," *Phys. Rev. B*, vol. 66, no. 12, p. 125207, Sep. 2002.
- [62] J. T. L. Thong, W. K. Choi, and C. W. Chong, "TMAH etching of silicon and the interaction of etching parameters," *Sensors Actuators A Phys.*, vol. 63, no. 3, pp. 243–249, Dec. 1997.
- [63] J. A. Thornton and D.W. Hoffman, "The compressive stress transition in Al, V, Zr, Nb and W metal films sputtered at low working pressures," *Thin Solid Films*, vol. 45, pp. 387–396, 1977.
- [64] J. A. Thornton and D.W. Hoffman, "Stress related effects in thin films," *Thin Solid Film*, vol. 171, pp. 5–31, 1989.
- [65] J. Kim, S. W. Bedell, and D. K. Sadana, "Improved germanium n⁺/p junction diodes formed by coimplantation of antimony and phosphorus," *Appl. Phys. Lett.*, vol. 98, no. 8, p. 082112, 2011.
- [66] G. Thareja, S. Chopra, B. Adams, Y. Kim, S. Moffatt, K. Saraswat, and Y. Nishi, "High n-type antimony dopant activation in germanium using laser annealing for n⁺/p junction diode," *IEEE Electron Device Lett.*, vol. 32, no. 7, pp. 838–840, 2011.
- [67] T. Krishnamohan, D. Kim, T. V. Dinh, A. Pham, B. Meinerzhagen, C. Jungemann, and K. Saraswat, "Comparison of (001), (110) and (111) uniaxial- and biaxial- strained-Ge and strained-Si PMOS DGFETs for all channel orientations: mobility enhancement, drive current, delay and off-state leakage," *IEEE. IEDM. Tech. Dig.*, pp. 899–892, 2008.

- [68] G. F. Burkhard, E. T. Hoke, and M. D. McGehee, "Accounting for interference, scattering, and electrode absorption to make accurate internal quantum efficiency measurements in organic and other thin solar cells," *Adv. Mater.*, vol. 22, no. 30, pp. 3293–7, Aug. 2010.
- [69] S. A. Claussen, E. Tasyurek, J. E. Roth, and D. A. B. Miller, "Measurement and modeling of ultrafast carrier dynamics and transport in germanium/silicon-germanium quantum wells," *Opt. Express*, vol. 18, no. 25, pp. 25596–607, Dec. 2010.
- [70] R. A. Minamisawa, M. J. Süess, R. Spolenak, J. Faist, C. David, J. Gobrecht, K. K. Bourdelle, and H. Sigg, "Top-down fabricated silicon nanowires under tensile elastic strain up to 4.5%," *Nat. Commun.*, vol. 3, p. 1096, Oct. 2012.
- [71] D. Nam, D. S. Sukhdeo, J.-H. Kang, J. Petykiewicz, J. H. Lee, W. S. Jung, J. Vučković, M. L. Brongersma, and K. C. Saraswat, "Strain-induced pseudoheterostructure nanowires confining carriers at room temperature with nanoscale-tunable band profiles," *Nano Lett.*, vol. 13, pp. 3118–3123, Jun. 2013.
- [72] M. J. Süess, R. Geiger, R. A. Minamisawa, G. Schieflier, J. Frigerio, D. Chrastina, G. Isella, R. Spolenak, J. Faist, and H. Sigg, "Analysis of enhanced light emission from highly strained germanium microbridges," *Nat. Photon.*, vol. 7, pp. 466–472, 2013.
- [73] J. Jain, D. Ly-Gagnon, K. Balram, J. S. White, M. L. Brongersma, D. A. B. Miller, and R. T. Howe, "Tensile-strained germanium-on-insulator substrate fabrication for silicon-compatible optoelectronics," *Opt. Mat. Express*, vol. 1, no. 6, pp. 1121–1126, 2011.
- [74] C. O. Chui, H. Kim, D. Chi, P. C. McIntyre, and K. C. Saraswat, "Nanoscale Germanium MOS dielectrics—part II: high- κ gate dielectrics," *IEEE Trans. Electron Devices*, vol. 53, no. 7, pp. 1509–1516, 2006.
- [75] J. J. Sheng, D. Leonhardt, S. M. Han, S. W. Johnston, J. G. Cederberg, and M. S. Carroll, "Empirical correlation for minority carrier lifetime to defect density profile in germanium on silicon grown by nanoscale interfacial engineering," *J. Vac. Sci. Technol. B Microelectron. Nanom. Struct.*, vol. 31, no. 5, p. 051201, 2013.
- [76] I. Åberg, C. N. Chléirigh, and J. L. Hoyt, "Ultrathin-body strained-Si and SiGe heterostructure-on-insulator MOSFETs," *IEEE Trans. Electron Devices*, vol. 53, no. 5, pp. 1021–1029, 2006.

- [77] A. M. Nayfeh, “Heteroepitaxial growth of relaxed germanium on silicon,” *Ph.D. dissertation*, Dept. Elec. Eng., Stanford Univ., Stanford, CA, June, 2006.
- [78] N. Tas, T. Sonnenberg, H. Jansen, R. Legtenberg, and M. Elwenspoek, “Stiction in surface micromachining,” *J. Micromech. Microeng.*, vol. 6, pp. 385-397, 1996.
- [79] I. De Wolf, “Micro-Raman spectroscopy to study local mechanical stress in silicon integrated circuits,” *Semicond. Sci. Technol.*, vol. 11, no. 2, pp. 139–154, Feb. 1996.
- [80] I. De Wolf, H. E. Maes, and S. K. Jones, “Stress measurements in silicon devices through Raman spectroscopy: Bridging the gap between theory and experiment,” *J. Appl. Phys.*, vol. 79, no. 9, p. 7148, 1996.
- [81] H. Koyama and P. Fauchet, “Laser-induced thermal effects on the optical properties of free-standing porous silicon films,” *J. Appl. Phys.*, vol. 87, no. 4, p. 1788, 2000.
- [82] Y. Kawamura, K. C. Y. Huang, S. V. Thombare, S. Hu, M. Gunji, T. Ishikawa, M. L. Brongersma, K. M. Itoh, and P. C. McIntyre, “Direct-gap photoluminescence from germanium nanowires,” *Phys. Rev. B*, vol. 86, no. 3, p. 035306, Jul. 2012.
- [83] F. H. Pollak and M. Cardona, “Piezoelectronreflectance from Ge, GaAs, and Si,” *Phys. Rev.*, vol. 172, no.3, August, 1968.
- [84] H. Kroemer, “A proposed class of hetero-junction injection lasers,” *Proc. IEEE*, vol. 51, no. 12, pp. 1782–1783, Dec. 1963.
- [85] F. Capasso, S. Luryi, W. Tsang, C. Bethea, and B. Levine, “New transient electrical polarization phenomenon in sawtooth superlattices,” *Phys. Rev. Lett.*, vol. 51, no. 25, pp. 2318–2321, Dec. 1983.
- [86] F. Qian, Y. Li, S. Gradecak, H.-G. Park, Y. Dong, Y. Ding, Z. L. Wang, and C. M. Lieber, “Multi-quantum-well nanowire heterostructures for wavelength-controlled lasers,” *Nat. Mater.*, vol. 7, no. 9, pp. 701–6, Sep. 2008.
- [87] A. Polman and H. A. Atwater, “Photonic design principles for ultrahigh-efficiency photovoltaics,” *Nat. Mater.*, vol. 11, no. 3, pp. 174–7, Mar. 2012.
- [88] X. Wang, G. Koleilat, J. Tang, and H. Liu, “Tandem colloidal quantum dot solar cells employing a graded recombination layer,” *Nat. Photonics*, vol. 5, no. August, pp. 480–484, 2011.

- [89] H. Kroemer, "Heterostructure bipolar transistors and integrated circuits," *Proc. IEEE*, vol. 70, no. 1, pp. 13–25, 1982.
- [90] I. Hayashi, M. B. Panish, P. W. Foy, and S. Sumski, "Junction lasers which operate continuously at room temperature," *Appl. Phys. Lett.*, vol. 17, no. 3, p. 109, 1970.
- [91] B. Ellis, M. A. Mayer, G. Shambat, T. Sarmiento, J. Harris, E. E. Haller, and J. Vučković, "Ultralow-threshold electrically pumped quantum-dot photonic-crystal nanocavity laser," *Nat. Photonics*, vol. 5, no. April, pp. 297–300, 2011.
- [92] A. Y. Cho, "Film deposition by molecular-beam techniques," *J. Vac. Sci. Technol.*, vol. 8, no. 5, p. S31, Sep. 1971.
- [93] H. Asai and K. Oe, "Energy band-gap shift with elastic strain in $\text{Ga}_x\text{In}_{1-x}\text{P}$ epitaxial layers on (001) GaAs substrates," *J. Appl. Phys.*, vol. 54, no. 4, p. 2052, Apr. 1983.
- [94] J. Greil, A. Lugstein, C. Zeiner, G. Strasser, and E. Bertagnolli, "Tuning the electro-optical properties of germanium nanowires by tensile strain," *Nano Lett.*, vol. 12, no. 12, pp. 6230–4, Dec. 2012.
- [95] G. Signorello, S. Karg, M. T. Björk, B. Gotsmann, and H. Riel, "Tuning the light emission from GaAs nanowires over 290 meV with uniaxial strain," *Nano Lett.*, vol. 13, no. 3, pp. 917–24, Mar. 2013.
- [96] J. Feng, X. Qian, C.-W. Huang, and J. Li, "Strain-engineered artificial atom as a broad-spectrum solar energy funnel," *Nat. Photon.*, vol. 6, no. 12, pp. 866–872, Nov. 2012.
- [97] K. Kash, B. Van der Gaag, D. Mahoney, A. S. Gozdz, L. T. Florez, J. P. Harbison, and M. D. Sturge, "Observation of quantum confinement by strain gradients," *Phys. Rev.* vol. 67, no. 10, 1991.
- [98] M. Huang, C. S. Ritz, B. Novakovic, D. Yu, Y. Zhang, F. Flack, D. E. Savage, P. G. Evans, I. Knezevic, F. Liu, and M. G. Lagally, "Mechano-electronic superlattices in silicon nanoribbons," *ACS Nano*, vol. 3, no. 3, pp. 721–727, 2009.
- [99] H. Kroemer, "Quasi-electric and quasi-magnetic fields in nonuniform semiconductors," *RCA Rev.*, 1957.

- [100] W. T. Tsang, "Extremely low threshold (AlGa)As graded-index waveguide separate-confinement heterostructure lasers grown by molecular beam epitaxy," *Appl. Phys. Lett.*, vol. 40, no. 3, p. 217, 1982.
- [101] S. R. Chinn, P. S. Zory, and A. R. Reisinger, "A model for GRIN-SCH-SQW diode lasers," *IEEE J. Quantum Electron.*, vol. 24, no. 11, pp. 2191–2214, 1988.
- [102] H.-G. Park, S.-H. Kim, S.-H. Kwon, Y.-G. Ju, J.-K. Yang, J.-H. Baek, S.-B. Kim, and Y.-H. Lee, "Electrically driven single-cell photonic crystal laser.," *Science*, vol. 305, no. 5689, pp. 1444–7, Sep. 2004.
- [103] P. Waltereit, O. Brandt, A. Trampert, H. Grahn, J. Menniger, M. Ramsteiner, M. Reiche, and K. Ploog, "Nitride semiconductors free of electrostatic fields for efficient white light-emitting diodes," *Nature*, vol. 406, no. 6798, pp. 865–8, 2000.
- [104] T. L. Koch and U. Koren, "Semiconductor photonic integrated circuits," *IEEE J. Quantum Electron.*, vol. 27, no. 3, pp. 641–653, Mar. 1991.
- [105] P. M. Asbeck, K. C. Wang, D. L. Miller, G. J. Sullivan, N. H. Sheng, E. A. Sovero, and J. A. Higgins, "Heterojunction Bipolar Transistors for Microwave and Millimeter-Wave Integrated Circuits," *Microwave Millimeter-Wave Integr. Circuits.*, vol. 83, no. 1. 1987.